Enhancing the Durability of Bridge Decks by Incorporating Microencapsulated Phase Change Materials (PCMs) in Concrete

Final Report
October 2025

Principal Investigator: Sumanta Das

Civil and Environmental Engineering
University of Rhode Island

Authors
Rakesh Paswan; He-Wen-Xuan Li; Sumanta Das

Sponsored By
Transportation Infrastructure Durability Center

A report from
University of Rhode Island
Department
Civil and Environmental Engineering
2 E Alumni Ave, Kingston, RI 02881
Phone: 401-874-5637
Website: https://web.uri.edu/cve/

About the Transportation Infrastructure Durability Center

The Transportation Infrastructure Durability Center (TIDC) is the 2018 US DOT Region 1 (New England) University Transportation Center (UTC) located at the University of Maine Advanced Structures and Composites Center. TIDC's research focuses on efforts to improve the durability and extend the life of transportation infrastructure in New England and beyond through an integrated collaboration of universities, state DOTs, and industry. The TIDC is comprised of six New England universities, the University of Maine (lead), the University of Connecticut, the University of Massachusetts Lowell, the University of Rhode Island, the University of Vermont, and Western New England University.

U.S. Department of Transportation (US DOT) Disclaimer

Acknowledgements

Funding for this research is provided by the Transportation Infrastructure Durability Center at the University of Maine under grant 69A3551847101 from the U.S. Department of Transportation's University Transportation Centers Program.

Technical Report Documentation Page

1. Report No.	**2. Government Accession No.**	**3. Recipient Catalog No.**
4 Title and Subtitle Enhancing the Durability of Bridge Decks by Incorporating Microencapsulated Phase Change Materials (PCMs) in Concrete		**5 Report Date 10/17/2025** **6 Performing Organization Code**
7. Author(s) Rakesh Paswan https://orcid.org/0000-0001-5357-3492 He-Wen-Xuan Li https://orcid.org/0000-0003-4162-5026 Sumanta Das https://orcid.org/0000-0001-5339-7708		**8 Performing Organization Report No.**
9 Performing Organization Name and Address University of Rhode Island, 45 Upper College Rd, Kingston, RI 02881		**10 Work Unit No. (TRAIS)** **11 Contract or Grant No.**
12 Sponsoring Agency Name and Address U.S. Department of Transportation		**13 Type of Report and Period Covered** **14 Sponsoring Agency Code**
15 Supplementary Notes		

16 **Abstract:** In cold climate regions, repeated freezing and thawing during the winter months causes concrete on bridges and road surfaces to crack and deteriorate over time. This damage shortens the service life of transportation infrastructure and increases maintenance costs. To address this problem, this project explored the use of microencapsulated phase change materials (PCMs) in concrete. These materials can store and release heat as they freeze and melt. When temperatures drop, the PCMs release stored heat, helping to keep the concrete slightly warmer and reducing the number of freeze–thaw cycles that cause cracking and surface damage. A series of laboratory experiments was carried out to test different PCM types and amounts in concrete mixtures. The project also used machine learning tools to analyze the experimental data and predict how different PCM combinations would perform under various temperature conditions. The results showed that adding PCMs to concrete can significantly reduce freeze–thaw damage and improve long-term durability. The research provides a new, data-driven approach for designing more resilient and longer-lasting concrete for bridges and pavements in cold climates.

17 Key Words		**18 Distribution Statement** No restrictions. This document is available to the public through	
19 Security Classification (of this report) Unclassified	**20 Security Classification (of this page)** Unclassified	**21 No. of pages**	**22 Price**

Form DOT F 1700.7 (8-72)

Contents

List of Figures 4
List of Tables 6
List of Key Terms 6
Abstract 8
Chapter 1: Introduction and Background 9
1.1 Project Motivation 9
1.2 Research, Objectives, and Tasks 9
1.3 Report Overview 10
Chapter 2: Methodology 10
2.1 Experimental Methods 10
2.2 Methodology for Simulation/Data-Driven Approach 16
Chapter 3: Results and Discussion 25
3.1 Experimental Results 25
3.2 Add sections/headings as needed 41
Chapter 4: Conclusions and Recommendations 48
References 49

List of Figures

Figure 1. Particle size distribution of OPC, MPCM, and sand.

Figure 2. DSC Thermogram of MPCM showing normalized heat flow as a function of temperature, illustrating both the cooling and heating cycles.

Figure 3. Temperature – time profile in freeze-thaw chamber

Figure 4. Segmentation workflow applied to raw XRT images for quantifying and analyzing pores and cracks in mortars specimens before and after freeze-thaw cycles (a1-a5 illustrates 3D volumes, while b1-b5 depicts 2D cross-sections)

Figure 5 A schematic of the FE-based numerical homogenization to obtain the effective thermal properties for the four considered length scales: (a) HHCP scale, (b) mortar scale, (c) concrete scale, and (4) bridge scale.

Figure 6 A schematic of the bridge deck geometry and the thermal interactions between the bridge deck and the surroundings.

Figure 7 A schematic of the main contributions of the thermal interaction between the bridge deck and the surrounding

Figure 8 SHAP river flow diagram which illustrates how the additive attribution assigns importance to each feature through the computation of ϕ_i for a given training sample (the blue curve).

Figure 9. DSC heat flow vs. temperature profiles for (a) control, (b) PCM-10, and (c) PCM-20 mortar samples.

Figure 10. Ice content as a function of temperature in mortar samples.

Figure 11. (a) Conversion and (b) conversion rate of MPCM-enhanced mortar samples during freezing.

Figure 12. Impact of MPCM dosage on the initial mechanical properties of cementitious composites: (a) percentage loss in compressive and flexural strength and (b) relative dynamic elastic modulus with varying MPCM dosage.

Figure 13. Comparative mechanical degradation of control mortar and MPCM incorporated mortars under progressive freeze-thaw cycles: (a) compressive strength, (b) relative compressive strength loss, (c) flexural strength, and (d) relative flexural strength loss with increasing number of freeze-thaw cycles.

Figure 14. Comparative analysis of relative dynamic modulus of elastic (RDME) across freeze-thaw cycles for control and MPCM-infused mortars.

Figure 15. Visual comparison of control and MPCM-integrated mortar samples before and after exposure to freeze-thaw cycles.

Figure 16. 2D images of mortar samples illustrating progressive freeze-thaw damage under X-ray tomography after 0, 216, and 324 freeze-thaw cycles.

Figure 17. Progressive freeze-thaw damage in control mortar visualized in 3D. Greyscale images showing: (a-1) the initial meso-structure before any cycles, (b-1) after 216 cycles, and (c-1) after 324 cycles. Corresponding, segmented visualization of pores and cracks is presented in a-2, b-2, and c-2 on greyscale images, illustrating the freeze-thaw-induced damage progression around the solid meso-structural features. 3D views of the pores and damage evolution without the greyscale solid phases are provided in a-3, b-3, and c-3, while b-4 and c-4 exclusively detail the significant growth of freeze-thaw induced cracks through the cycles, particularly highlighting the ITZ as a critical zone of damage.

Figure 18. Visualization of reduced freeze-thaw damage in PCM-10 mortar in 3D. The greyscale images showing the PCM-10 mortar's meso-structure at (a-1) zero, (b-1) after 216 cycles, and (c-1) following 324 cycles, respectively. Compared to the control, these images, along with their segmented counterparts a-2, b-2, and c-2, reveal a less severe development of pores and cracks, suggesting the mitigating effects of MPCM against freeze-thaw damage. The 3D visualizations of pores and damage progression, depicted in a-3, b-3, and c-3, further demonstrate the mortar's resilience, with a noticeably lower extent of cracking and porosity expansion. Images b-4 and c-4, which isolate the freeze-thaw-induced cracks, confirm the limited progression of structural deterioration over time, evidencing the MPCM's role in enhancing the durability of the mortar against freeze-thaw cycles.

Figure 19. The durability of PCM-20 mortar against freeze-thaw cycles illustrated through 3D XRT images. Greyscale images represent: (a-1) the intact meso-structure before freeze-thaw cycles, (b-1) after 216 cycles, and (c-1) following 324 cycles, respectively. Segmented visualizations a-2, b-2, and c-2 show the pores and cracks in the greyscale image demonstrating minimal change of pores and crack volumes after freeze-thaw cycles. The 3D renderings a-3, b-3, and c-3 demonstrate the 3D pore structure evolution. Figure c-4 displays the freeze-thaw-induced cracks isolated from the pore structure inherently present in the meso-structure where minimal crack development was observed. No such image is provided here for 216 cycles as no crack was detected after image segmentation. The overarching outcome indicates that PCM-20 offers robust protection, effectively preserving the mortar's meso-structure even after extensive freeze-thaw exposure.

Figure 20. Evolution of (a) percentage of pore/crack volume and (b) percentage change in pore/crack volume in mortar samples with increasing freeze-thaw cycles. Both graphs underscore the enhanced durability imparted by MPCM, with PCM-20 exhibiting the most significant resistance to freeze-thaw-induced damage. (Note: ns $p > 0.05$; * $p \leq 0.05$; ** $p \leq 0.01$; *** $p \leq 0.001$; **** $p \leq 0.0001$).

Figure 21 The effectiveness of the proposed MPCMC protective layer by comparing the control case with respect to an exemplary layer with design parameters: $d_{\mathrm{pcm}} = 8\mathrm{e}^{-6}\mathrm{m}$, $v_{\mathrm{pcm}} = 0.05$, $\rho_{\mathrm{eff}} = 2213$ kg/m^3, $k_{\mathrm{eff}} = 1.21\mathrm{W/m{\cdot}K}$, $C_{\mathrm{peff}} = 908.9\mathrm{J/kg{\cdot}K}$, $t_{\mathrm{ol}} = 0.036\mathrm{m}$, $H = 250\mathrm{kJ/kg{\cdot}K}$, and $T_t = -5$. (a) The temperature field without the MPCMC; (b) the temperature field with the exemplary MPCMC; (c) a comparison of the temperature-time histories with and without the MPCMC layer with close-ups that illustrate the FTC reduction about the freezing temperature T_f. Figure c1 shows the overall temperature-time histories. Figures c2 and c3 show close-ups of the Figure c1 at two different time ranges.

Figure 22 A schematic of the main contributions of the thermal interaction between the bridge deck and the surrounding: (a) learning curve of the tuned model; (b) tuned model accuracy

Figure 23 (a) SHAP summary plot and (b) SHAP violin plot for each input from the trained NN model

Figure 24. SHAP river flow plot for FTC counts using the trained NN model.

Figure 25 Generalizability of the Intelligent Model: wind-rose plot for (a) training inputs; (b) exploration inputs (interpolation and extrapolation); performance of the trained model on (c) test dataset, (d) interpolated inputs; (e) extrapolation inputs.

List of Tables

Table 1: Thermo-physical properties of MPCM used in the study

Table 2: Mortar mixture proportion (kg/m^3)

Table 3. A summary of the thermal properties and the geometrical features of the materials

Table 4. Effective thermal properties at the three length scales

Table 5. A summary of the physical constants used in the trial experiments

Table 6: Mean enthalpy of fusion values with standard deviations as indicators of ice content obtained during the ice-to-water phase transition across four replicate samples

List of Key Terms

Phase Change Material (PCM):
A substance that absorbs or releases thermal energy during a phase transition (typically solid–liquid) to regulate temperature. When incorporated into cementitious materials, PCMs help moderate temperature fluctuations and reduce freeze–thaw damage.

Microencapsulated Phase Change Material (MPCM):
A PCM enclosed within a protective polymer shell that allows for stable dispersion within cementitious matrices. The microcapsule prevents leakage during melting and enhances material compatibility.

Freeze–Thaw Cycle (FTC):
A repetitive process in which water within concrete freezes and thaws due to temperature variations, causing internal stresses, cracking, and durability loss over time.

Concrete Overlay:
A layer of concrete applied to the surface of existing bridge decks or pavements to restore or enhance structural and durability performance. In this project, overlays are designed with PCMs to mitigate freeze–thaw damage.

Latent Heat:
The amount of heat absorbed or released by a material during a phase change without changing its temperature. In PCMs, this property enables energy storage and thermal regulation.

Transition Temperature:
The temperature range at which a PCM undergoes a phase change (from solid to liquid or vice versa). This determines the effectiveness of PCMs in moderating concrete temperature during freezing conditions.

Machine Learning (ML):
A subset of artificial intelligence involving algorithms that learn from data to make predictions or decisions. ML models were used in this project to predict and optimize PCM-enhanced material performance.

Multiscale Simulation:
A computational approach that evaluates material behavior by linking information from multiple length scales—ranging from microstructure to structural response—to estimate effective thermal and mechanical properties.

Shapley Additive Explanations (SHAP):
An interpretability method used in machine learning to quantify the contribution of each input variable to the model's predictions. In this project, SHAP analysis identified the dominant design parameters influencing freeze–thaw mitigation.

Abstract

In cold climate regions, repeated freezing and thawing during the winter months causes concrete on bridges and road surfaces to crack and deteriorate over time. This damage shortens the service life of transportation infrastructure and increases maintenance costs. To address this problem, this project explored the use of microencapsulated phase change materials (PCMs) in concrete. These materials can store and release heat as they freeze and melt. When temperatures drop, the PCMs release stored heat, helping to keep the concrete slightly warmer and reducing the number of freeze–thaw cycles that cause cracking and surface damage. A series of laboratory experiments was carried out to test different PCM types and amounts in concrete mixtures. The project also used machine learning tools to analyze the experimental data and predict how different PCM combinations would perform under various temperature conditions. The results showed that adding PCMs to concrete can significantly reduce freeze–thaw damage and improve long-term durability. The research provides a new, data-driven approach for designing more resilient and longer-lasting concrete for bridges and pavements in cold climates.

Chapter 1: Introduction and Background

1.1 Project Motivation

The condition of the nation's transportation infrastructure remains a major concern across the United States, particularly in regions with harsh winter climates. Despite notable improvements in recent years, Rhode Island continues to have one of the highest percentages of structurally deficient bridges in the country. The frequent cycles of freezing and thawing during the winter months contribute significantly to this deterioration, causing cracking, surface scaling, and progressive loss of strength in concrete bridge decks and pavements.

To address this persistent challenge, the concept of using microencapsulated phase change materials (PCMs) within concrete has emerged as a promising strategy. PCMs absorb and release heat as they change phase, helping to moderate temperature fluctuations within the concrete. When incorporated appropriately, they can reduce the number and severity of freeze–thaw cycles that the concrete experiences, thereby minimizing damage and extending service life.

This project was motivated by the need to identify practical and effective solutions for enhancing the durability of bridge infrastructure in cold regions. The integration of thermal energy–storing materials such as PCMs offers a novel pathway toward creating self-regulating, freeze–thaw–resistant concrete systems. By advancing this approach, the work contributes to improving the resilience, safety, and sustainability of transportation networks in Rhode Island and other northeastern states.

1.2 Research, Objectives, and Tasks

The primary objectives of this project were twofold. The first objective was to develop phase change material (PCM)–incorporated cementitious composites with significantly improved resistance to freeze–thaw cycles and enhanced crack-tolerance behavior. To achieve this goal, PCM-modified cementitious mixtures were designed and evaluated to determine the influence of PCM dosage, transition temperature, and mixture proportions on thermal and mechanical performance. The work also examined the durability of these composites under repeated freeze–thaw exposure, as well as the relationship between internal material structure and overall engineering properties.

The second objective was to establish a computational and machine learning–based materials design framework for PCM-enhanced concrete overlays used in bridge decks and pavements. This framework integrates predictive modeling and simulation tools to estimate the thermal and mechanical response of overlays under varying environmental conditions. The machine learning models were trained using performance data to identify optimal PCM type, dosage, and transition temperature, enabling rational design of overlays that minimize freeze–thaw damage and extend service life in cold-region transportation infrastructure.

1.3 Report Overview

This report documents the development, evaluation, and analysis of phase change material (PCM)–incorporated cementitious composites and concrete overlays aimed at improving freeze–thaw resistance in cold-region infrastructure. It presents the experimental methodology used to characterize the thermal and mechanical behavior of PCM-modified cementitious composites, followed by the simulation and machine learning approaches developed to model and predict the performance of PCM-enhanced overlays. The results and their interpretations are discussed in detail, highlighting the relationships between material composition, thermal response, and durability performance. The report concludes with key findings, implementation recommendations, and directions for future research to support broader adoption of PCM-based materials in transportation infrastructure.

Chapter 2: Methodology

2.1 Experimental Method

2.1.1 Source Materials and Characterization

The cement used in the experimental studies is commercial-grade ordinary Portland cement (OPC, Type I/II) conforming to ASTM C150 [1]. It has specific gravity of 3.15 and a fineness of 3660 cm^2/g. Quartz sand was used as fine aggregates. **Figure 1** illustrates the particle size of cement and sand, where the mean particle size of sand was 400 µm (d50), while for the OPC, it was 19.43 µm.

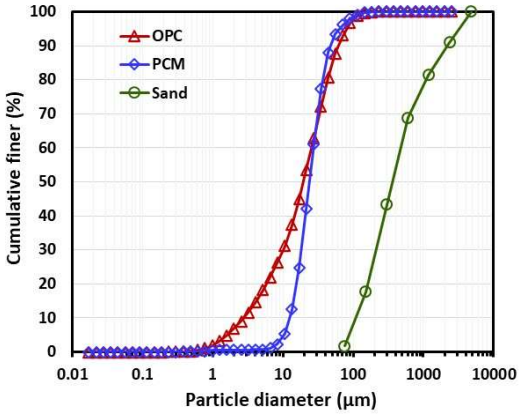

Figure 1. Particle size distribution of OPC, MPCM, and sand.

The MPCM used in this study, sourced from Microtek Laboratories Inc. (Ohio, USA), consists of 79.6% paraffin wax as the core material, encapsulated by a 17.4% hydrophobic melamine formaldehyde polymer shell. These MPCM were specifically designed for freezing applications like snow melting or deicing [2–4]. Micro-encapsulation is a process of enclosing PCM droplets in a spherical shell, which prevents leakage and ensures thermal and structural stability. In this study, we ensured that the MPCMs used were free from any paraffin leakage or adverse effects on the cement hydration process. This was verified through thermogravimetric analysis (TGA) performed on MPCM-integrated cementitious samples. The thermo-physical properties of MPCM used in the study is given in the **Table 1**. The MPCM had a density of 900 kg/m^3, and its mean particle size was 23.67 µm (d_{50}). The particle size distribution of MPCM is shown in **Figure 1**.

The thermal behavior of MPCM, including onset and peak temperatures as well as enthalpy changes, was analyzed using a DSC (Discovery DSC 25 by TA Instruments, USA). Figure 2 presents the resulting thermogram of the MPCM. During testing, the MPCM was subjected to controlled heating and cooling cycles in a nitrogen atmosphere, with a temperature range from -30°C to 40°C at a rate of 5°C/min. Approximately 10 mg of the MPCM sample was used for each test run. The transition temperature and enthalpy of fusion for heating and cooling, along with their standard deviations, are summarized in **Table 1 and Figure 2**, based on the average of four replicate measurements.

Table 1: Thermo-physical properties of MPCM used in the study

Properties of micro-encapsulated PCM	
Appearance	White/off white color
Form	Dry powder (≥ 97%)
Particle size (d_{50}, µm)	23.67
Density (kg/m³)	900
Thermal conductivity (W/m K)	0.20
Transition temperature (°C)	
Cooling cycle	-3.72
Heating cycle	7.66
Latent heat of fusion (J/g)	
Cooling cycle	196.26 ± 3.54
Heating cycle	194.45 ± 3.89

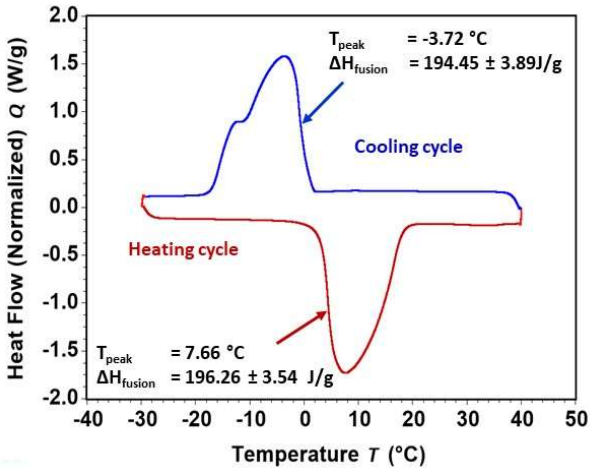

Figure 2. DSC Thermogram of MPCM showing normalized heat flow as a function of temperature, illustrating both the cooling and heating cycles. The peaks correspond to the thermal transitions of the MPCM, with the onset of melting (T_{peak}) and enthalpy of fusion (ΔH_{fusion}) annotated for both the endothermic and exothermic processes, along with their standard deviations from four replicate samples.

As shown in **Figure 2**, in the heating cycle, MPCMs absorbed heat (endothermic process) with a peak at 7.66 °C, indicative of melting, with an associated melting enthalpy of fusion of 196.26 ± 3.54 J/g. Upon cooling, the sample released heat (exothermic process), evident from the peak at -

3.72 °C, due to crystallization or solidification, with an associated crystallization enthalpy of fusion of 194.45 ± 3.89 J/g. It needs to be noted that during cooling, the heat release begins just above freezing, around 2°C, and extends down to approximately -10°C. This wide temperature range corresponds with typical freeze-thaw conditions in cold climates. By gradually releasing latent heat across this range, the MPCM can potentially stabilize the internal temperature of the mortar, delaying freezing and reducing rapid temperature fluctuations. This could potentially mitigate freeze-thaw damage and improve the long-term durability of the material. The difference in the melting and crystallization temperatures observed in MPCMs, as noted in **Figure 2**, can be explained by the phenomenon of supercooling. Paraffinic PCMs exhibit supercooling mainly due to their complex molecular structures and the mixture of hydrocarbons they contain, each with slightly different melting points. This compositional diversity can prevent uniform crystallization, effectively delaying nucleation—the critical process for solidification [5]. This delay continues until the supercooling reaches a level that energetically favors nucleation, causing the material to crystallize at a significantly lower temperature. This results in a notable temperature gap between the endothermic melting peak and the exothermic crystallization peak. Nevertheless, the comparable magnitudes of the heat of fusion for both processes indicate a nearly reversible phase transition. To ensure a consistent evaluation between control and MPCM-incorporated mortar, the workability of the mixture was optimized through the incorporation of a superplasticizer. MasterGlenium 3030, a polycarboxylate-based superplasticizer, was used in this study and sourced from Master Builders Solutions Admixtures US, LLC (Pennsylvania, USA).

2.1.2 Mixture Proportions and Sample Preparation

This study investigates five mortar formulations with a consistent mass-based water-to-cement ratio of 0.4. These formulations incorporated different proportions of MPCM: 0%, 5%, 10%, 15%, and 20% by volume as sand replacement. MPCM content exceeding 20% was excluded as it showed significantly lower strength compared to the requirements for concrete/pavement applications [6,7]. Previous studies [6,7] examining MPCM content greater than 20% by volume revealed substantial microstructural changes, including increased porosity and critical pore diameter. These alterations adversely affected the mechanical strength and overall performance of cement paste and mortar when subjected to freeze-thaw cycles. Mortar samples were prepared using a planetary mixer. Detailed mix design is outlined in **Table 2.**

Table 2: Mortar mixture proportion (kg/m^3)

Mixture	Quantity (kg/m^3)				
	Cement	Sand	MPCM	water	Superplasticizer
Control mortar		1325	0.0		0.28
PCM-5		1259	22.5		0.42
PCM-10	696	1193	45.0	279	0.56
PCM-15		1126	67.5		0.70
PCM-20		1060	90.0		0.84

The mixture process involved initial dry mixing of cement and MPCM at low speed for 1 minute. Premixed water and superplasticizer were then added during the next 30 seconds, followed by an addition of sand particles for another 30 seconds of mixing. The final mixture was blended for 1 minute at low speed and next 30 seconds at medium speed. The fresh prepared mortar was cast into a plastic mold, followed by tamping and vibration on the table for 10 ± 5 seconds until a plain

finished surface was obtained. Superplasticizer content was adjusted to achieve a consistent flow table test diameter of 130 ± 5 mm (as per ASTM C1437 [8]). The prepared samples were sealed and allowed to cure for 24 hours. Subsequently, the samples were demolded and kept in a chamber with temperature 23 ± 2°C and relative humidity 97% for 56 days before implementing freeze-thaw cycles.

2.1.3 Freeze – thaw Cycles

Freeze-thaw experiments on control and MPCM-integrated mortars were conducted as per ASTM C666 [9], specifically following test procedure A. This procedure is typically considered more rigorous due to the continuous saturation of test specimens in water throughout the freeze-thaw cycles, thereby creating a more severe testing environment. Following the standard guidelines, prismatic beam (160 × 40 × 40 mm) and cube (50 × 50 × 50 mm) specimens were meticulously subjected to a temperature range of -18 °C to 14 °C up to 324 freeze-thaw cycles. The freeze-thaw cycles were designed to last between 2 and 5 hours to ensure sufficient time for both freezing and thawing phases, facilitating a thorough evaluation of the materials' durability. All specimens were soaked for 48 hours to achieve full saturation (100% moisture) before testing. The typical temperature – time profile from the freeze-thaw test is depicted in **Figure 3**, which closely aligns with the temperature amplitude defined by the standard [9]. The chamber maintained a relative humidity above 65% during the sub-zero phases (below 0°C). For each case, three replicate samples were subjected to freeze-thaw cycles. Prior to the initiation of the tests, all specimens underwent a 48-hours soaking period in water. The damage assessment of exposed specimens involved measuring the RDME, as well as flexural and compressive strengths at 0, 108, 216, and 324 cycles as detailed in the forthcoming sections.

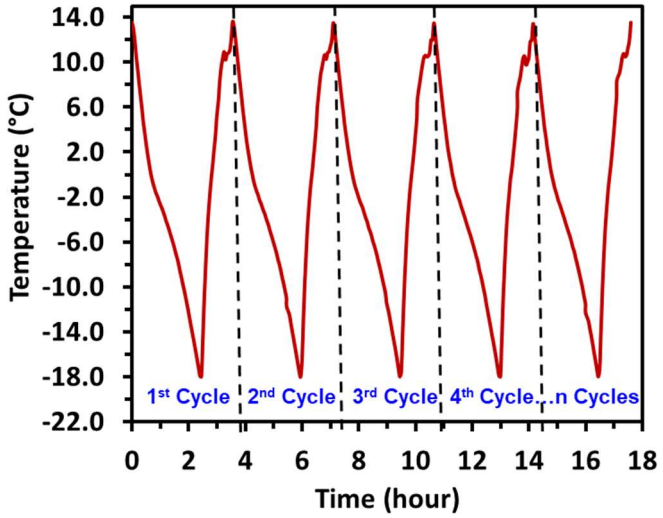

Figure 3. Temperature – time profile in freeze-thaw chamber

2.1.4 Materials Characterization Methods for MPCM-integrated Mortars

Analyzing Thermal Characteristics of MPCM-integrated Mortars Using Differential Scanning Calorimetry (DSC)

The thermal analysis of the materials, including onset and peak temperatures as well as enthalpy changes, were measured using DSC (Discovery DSC 25 by TA Instruments, USA). The mortar samples were sealed in an aluminum pan. Prior to testing, the samples underwent a 48-hour immersion in water to attain complete saturation, which is essential to capture the accurate freeze-thaw event in cementitious composites. The DSC protocol commenced with the samples being stabilized at 10°C for 2 minutes, followed by cooling down to -35°C, then kept at -35°C for another 2 minutes, and finally reheated to 10°C, all conducted under an inert nitrogen atmosphere with both cooling and subsequent heating cycles proceeding at a constant rate of 5°C/min. To ensure the accuracy and representativeness of the DSC tests, multiple independent trials were conducted, with four samples tested for each measurement. Moreover, this approach is consistent with previous studies, such as those by Balapour et al. [4], Sharifi and Sakulich [10], and Farnam et al. [11], which also used multiple DSC tests to evaluate the thermal properties of MPCM-incorporated mortars successfully.

Compressive and Flexural Strength Assessment

For mechanical performance assessment, control, as well as MPCM-integrated mortar specimens, were subjected to compression and flexural (three-point bend) tests before applying any freeze-thaw cycles and after 108, 216, and 324 freeze-thaw cycles. The mechanical experiments were performed using a servo-controlled high-precision Shimadzu universal testing machine as per ASTM standards C109 [12] and C348 [13]. Three replicate mortar cubes (50 × 50 × 50 mm) and prismatic beams (160 × 40 × 40 mm) were employed for compression and flexure tests respectively for each material combination.

Evaluation of Relative Dynamic Modulus of Elasticity (RDME)

The RDME is a critical parameter for assessing the internal micro-damage of mortar specimens subjected to freeze-thaw cycles [14]. To evaluate the RDME of mortar specimens post freeze-thaw cycles, it suffices to record the initial ultrasonic velocity for each specimen and then remeasure the velocities after subjecting them to the cycles. The RDME is then inferred from the square of the velocity ratios, offering a streamlined yet effective approach to assessing freeze-thaw damage in mortar specimens. In this study, for each case, three replicate prism specimens (160 × 40 × 40 mm) were subjected to 0, 108, 216, and 324 freeze-thaw cycles to assess the evolution of RDME as the number of freeze-thaw cycles was increased.

Assessment of Damage Evolution Using X-Ray Tomography (XRT) and Image Analysis

The XRT analysis in this study was performed at the meso-scale, capturing key damage mechanisms like porosity changes and crack propagation. This meso-scale approach bridges the gap between microstructural evolution and macroscopic mechanical performance, providing insights into structural changes that significantly influence freeze-thaw durability in cementitious materials. Zeiss Xradia Versa 610 micro-tomography system was utilized to produce high-resolution images, employing 60 kV photon energy and 108 µA current. The resulting images, with dimensions of 994 × 1015 pixels, featured a target volume of a cylinder with a diameter of 3.93 mm and a height of 4.03 mm. The 3D volume from 2D images was reconstructed using Zeiss's Scout-and-Scan Control System Reconstructor software [15], while segmentation and subsequent analysis were conducted through Dragonfly image analysis software developed by Object Research Systems Inc. (Canada) [16]. Segmentation poses challenges due to minimal grayscale contrast as observed in several other studies on cementitious composites [17,18]. In this present study, the Otsu thresholding method was applied for phase segmentation in the mortar. This widely-used algorithm determines an optimal threshold based on the grayscale intensity histogram

[19], enabling accurate segmentation for subsequent analysis and characterization [20]. This segmentation approach, proven effective in previous studies [21–23], ensures accurate identification and distinction of pores/cracks within hydrated cement mortar. However, time-lapse tomography of same specimen subjected to varying freeze-thaw cycles exhibit misalignment, where a reference point, may shift between successive scans [24]. To mitigate this, we carefully designed the experiment to reduce misalignment from the outset. A reference point was established both on the specimen and sample stage to ensure uniform positioning. The entire specimen was scanned from top to bottom and specific slides (200) from top, bottom and sides of the cylindrical volumes were selected to obtain cubic region of interest (ROI) after each scan. This approach also ensures the removal of artifacts that may form due to the scanning of air within the X-ray field, leading to cleaner and more accurate analysis results [25].

Figure 4 illustrates the comprehensive workflow for quantifying and analyzing pores and cracks in both 3D and 2D XRT images. The process begins with the acquisition of raw datasets (a-1, b-1), which represent the initial scans of the specimens. To enhance the clarity of the images, a median filter was applied to the selected ROI, resulting in improved volume representations (a-2, b-2). This filtering technique was consistently applied across all XRT images collected at different time-lapse throughout the freeze-thaw cycles, ensuring uniformity and reliability in the data analysis. Following the filtering step, critical regions, including pores and cracks, were identified and segmented from the filtered images (a-3, b-3). This segmentation was performed using the lower threshold determined by Otsu's method, which effectively distinguishes the darker phases indicative of voids. Pores and cracks, being void without any mass to absorb radiation, appear as dark black regions in the XRT images and exhibit zero X-ray attenuation. This unique characteristic significantly aids in their effective segmentation, allowing for precise identification during analysis. In the XRT image (b-2), the pixel intensities correspond to various phases present within the matrix, which are intrinsically related to their respective X-ray attenuation coefficients. Higher gray intensity values are associated with denser regions, such as aggregates, unhydrated cement particles, and hydration products, while lower intensity values correspond to voids, including pores and cracks. The automatic threshold identified through the Otsu method was uniformly applied across all median-filtered images to maintain consistency in the segmentation process. Once the pores and cracks were successfully segmented, they were converted into multi-regions of interest (multi-ROIs). A multi-ROI expands upon the traditional ROI concept by accommodating multiple classes, thus facilitating the labeling and categorization of identified phases within the dataset. Utilizing a scalar generator function, measurements and analyses were performed on the multi-ROIs, allowing for the quantification of pore and crack volumes in both 2D and 3D representations. To achieve a more precise morphological assessment, the segmented cracks underwent further analysis based on their aspect ratios (a-5, b-5). All identified cracks displayed relatively small aspect ratios, ranging from 0 to 0.5, contributing valuable information regarding the structural integrity and durability of the cement mortar under investigation.

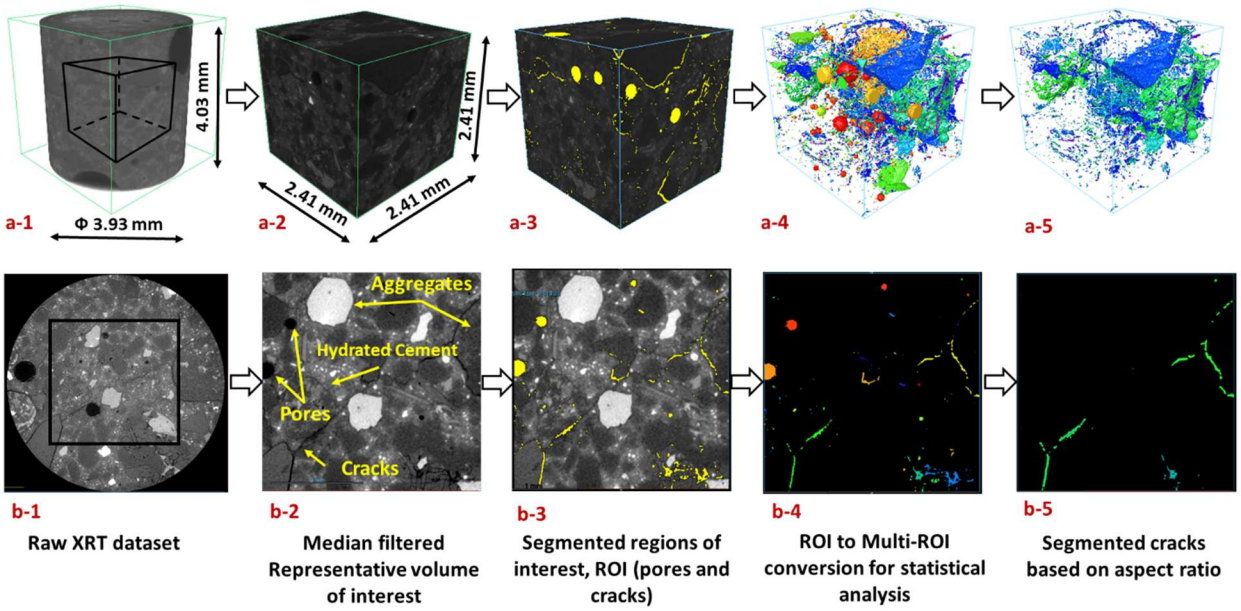

Figure 4. Segmentation workflow applied to raw XRT images for quantifying and analyzing pores and cracks in mortars specimens before and after freeze-thaw cycles (a1-a5 illustrates 3D volumes, while b1-b5 depicts 2D cross-sections)

2.2 Methodology for Simulation/Data-Driven Approach

2.2.1 Multiscale numerical simulation for simulating the effects of the proposed protective MPCM concrete layer

This section presents a simplified yet representative model that reflects the thermal interaction between the concrete bridge deck and the surroundings to generate thermal responses for FTC counting. Since the simulation involves multiple length scales, the thermal properties are calculated from homogenization at various length scales via FEA. The forthcoming sub-sections elaborate on the multiple length scales involved in the study, multiscale numerical homogenization to predict effective thermal properties of concrete, and the macro-scale simulation of thermal interactions and FTCs in the bridge deck that derives inputs from the multiscale homogenization.

Interactive Length scales

There are four scales involved in the homogenization process, which are (1) the homogenized hard cement paste (HHCP) scale, (2) the mortar scale, (3) the concrete scale, and (4) the bridge deck scale. These length scales are shown in Fig. 5.

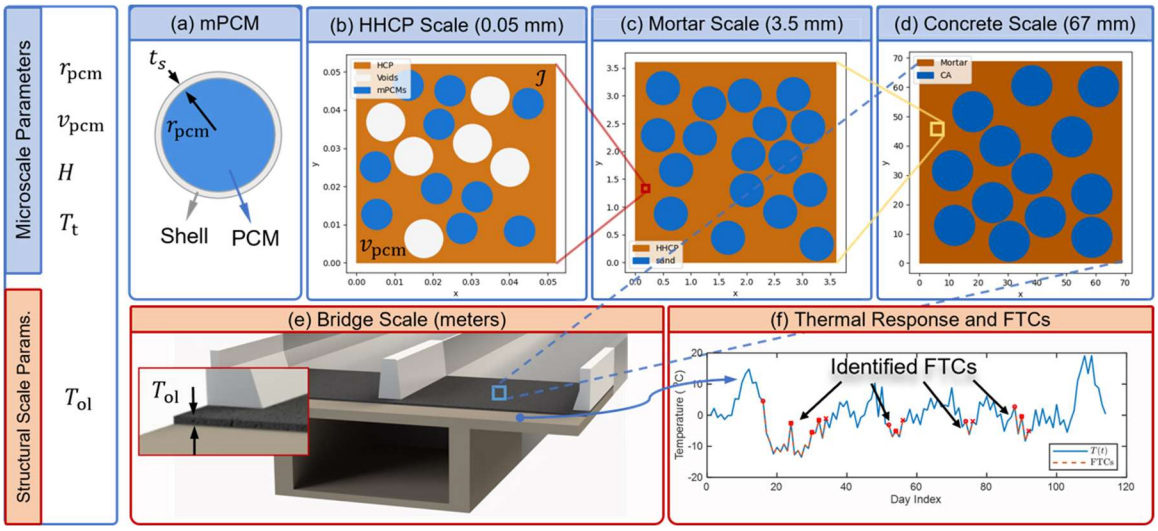

Fig. 5 A schematic of the FE-based numerical homogenization to obtain the effective thermal properties for the four considered length scales: (a) HHCP scale, (b) mortar scale, (c) concrete scale, and (4) bridge scale.

In each of the HHCP, mortar, and concrete scales, the simulation starts with the generation of representative volume elements using the known microstructural and thermal features of the matrix and inclusions followed by thermal analysis implementing periodic boundary condition so as to obtain the homogenized thermal properties of the RVE. The homogenized properties obtained for PCM-incorporated HCP are used as matrix properties in the mortar scale along with the thermal property of sand inclusions to obtain the homogenized properties of the mortar. Furthermore, the homogenized mortar properties are used as matrix properties in the concrete scale to obtain the homogenized concrete properties. Thereafter, the dynamic thermal simulations of bridge-environment interactions are conducted by implementing the homogenized PCM-incorporated concrete properties. The forthcoming sub-sections report on the multiscale numerical homogenization-based upscaling process to predict the FTCs in the concrete bridge deck with a PCM-concrete protective layer.

Multiscale Homogenization for Effective Thermal Property prediction

The first step to ensure an accurate calculation of the thermal properties of the MPCM-incorporated concrete is the homogenization across multiple length scales. A representative volume element (RVE) at each scale is generated with matrix and inclusion combinations. Based on the thermal response of the RVEs, effective thermal properties can be obtained. An illustration of the homogenization procedure is given in Fig. 5.

2D RVEs are generated using the Lobachevsky-Stillinger algorithm [26,27]. Such an algorithm ensures that no inclusion overlaps with one another. The RVE geometry is generated using a Python script at each length scale. A similar methodology has been successfully implemented in [28–30]. In this study, the size of the RVE is selected to be around six times the diameter of the largest inclusion based on an RVE-size sensitivity study at each length scale to ensure that the homogenized thermal properties are stabilized for the size of the RVE. 2D unit cells are considered here for computational efficiency. Periodic boundary conditions [31,32] are imposed in the RVE.

The imposition of the PBC ensures the continuity of the temperature field at the connected borers of any two arbitrary RVEs. Such an assumption shows sufficient accuracy in obtaining the homogenized thermal properties of cementitious materials [33].

A four-step homogenization of the MPCMC is followed in this paper to obtain the homogenized properties involving a combination of analytical and numerical homogenization. While analytical homogenization is employed to determine the effective homogenized densities across all length scales, as well as to ascertain the effective thermal conductivity and specific heat of the MPCM particles at the MPCM scale, the FEA-based numerical homogenization approach is utilized across all the three larger length scales—hardened cement paste, mortar, and concrete scale—to compute the effective thermal properties.

The first scale is the MPCM scale, as illustrated in Fig. 5 (a), where the only variation is contributed by the size of the MPCM while considering identical shell thickness to emulate the commercially available MPCMs. An analytical homogenization is used in this scale following the composite sphere approach detailed in [34]. After obtaining the analytically homogenized thermal properties of the MPCM, the effective thermal properties of the MPCMC are obtained via three length scales using sequential FEA-based numerical homogenization as detailed in the forthcoming Section 2.2.2. The first step involves the incorporation of MPCM into the hardened cement paste (HCP) matrix, where entrained air voids with diameters of 50 μm are present. The homogenization yields the homogenized HCP (HHCP), and it serves as the matrix material for the next step. Step 2 involves the homogenization of the HHCP and the sand as inclusions, which gives the effective thermal properties of the mortar scale. Finally, the introduction of the coarse aggregates into the homogenized mortar is conducted, and the resultant thermal properties serve as the thermal properties of the MPCMC for the bridge deck simulation.
For comparison, a three-step homogenization of the control concrete is conducted, without any incorporated MPCM as the HHCP does not have any effects from the MPCMs. The thermal properties of the inclusions and the matrix materials are illustrated in Table 3. The shape of the inclusions is considered spherical in this work since the geometry of the inclusion does not significantly alter the effective thermal conductivity. Moreover, it needs to be noted that generating non-circular inclusion, e.g., elliptical inclusions, is more computationally expensive for generating satisfactory target volume fraction. Hence, this works assumes spherical inclusions to expedite the numerical simulations while maintaining the accuracy of the homogenized thermal properties.

Table 3. A summary of the thermal properties and the geometrical features of the materials

Properties	**HCP**	**Sand**	**CA**	**Air Void**	**Shell**	**PCM**
$\boldsymbol{\lambda\ (W/m\ K)}$	0.75	2.80	2.30	-	0.19	0.20
$\boldsymbol{C_p\ (kJ/kg\ K)}$	2.60	1.15	2.30	-	2.60	2.00
$\boldsymbol{\rho\ (kg/m^3)}$ **(x 10^3)**	1.95	2.58	2.63	-	1.20	0.85
$\boldsymbol{diameter\ (mm)}$	-	0.6	13.8	0.01	-	$0.005 - 0.011$
$\boldsymbol{thickness}\ (\mu m)$	-	-	-	-	0.5	-

As for the shell formulated during the microencapsulation, we assume a commonly used polymethyl-methacrylate (PMMA) material with a constant thickness after investigating the studies on the shell's effects on the thermal performance [22-23,39–42]. The size of the air voids, sand, and coarse aggregate are adopted from [28,29] and the individual thermal properties are

obtained from [28,40–44]. The thermal properties of the paraffinic PCM are illustrated in ranges due to the investigation of how the variable thermal properties affect the FTCs. Additionally, the volume fraction of the MCPM as a sand replacement is in a range of 0 to 9%. For a detailed reason of the considered paraffinic PCM properties.

Effective thermal properties calculation

Steady-state thermal analyses are carried out on the generated RVE geometries. DC2D4 2D heat transfer elements are generated across the domain of interest. By stipulating the temperatures at the boundary with an arbitrary initial temperature field, the system temperature tends to be in equilibrium with volumetric reactive heat flux. Therefore, effective conductivity can be obtained based on the stipulated temperatures and the resultant heat flux. Such upscaling approach reflects the underlying size effects of the selected MPCM capsules. As for the effective specific heat capacity $C_{\mathrm{p,eff}}$, the reaction heat flux can be obtained at the nodes under the applied temperature gradient.

Similarly, the MPCMC's effective properties can be computed as well, with an additional consideration of the latent heat effects provided by the MPCM. The latent heat effect is modeled by an additional effective specific heat capacity as a function of temperature.
Whenever the temperature crosses T_{t}, an additional volumetric specific heat $v_{PCM}\rho_{\mathrm{eff}}H/\Delta T_p$ is induced due to the latent heat released/absorbed by the incorporated MPCM capsules, where the ρ_{c} denotes the density of the MPCM, H is the latent heat of fusion, and ΔT_{p} is the transition temperature. Following the above-mentioned procedure, the effective thermal properties are obtained at each length scale and the resultant range of effective thermal properties is summarized in Table 4. These ranges are arrived at based on the variations in the size and volume fraction of PCMs and These values serve as lower and upper bounds for design parameter exploration in the bridge deck simulations. The effect of the latent heat is considered, with the range of the effective concrete density of 2144 to 2294 kg/m^3. As a result, the effective volumetric latent heat $\frac{v_{PCM}\rho_{\mathrm{eff}}H}{\Delta T_p}$ lies in the range of 0 to 206.5 H kJ/m^3, depending on the latent heat capacity of the used PCMs.

Table 4. Effective thermal properties at the three length scales

Properties	**HHCP**		**Mortar**		**Concrete**	
	Min	Max	Min	Max	Min	Max
$\boldsymbol{\lambda\ (W/m\ K)}$	0.383	1.088	0.658	1.170	1.037	0.391
$\boldsymbol{C_p\ (kJ/kg\ K)}$	0.6	1.077	0.875	1.102	0.841	0.977

Thermal Response of Bridge Deck

While the previous section evaluates the effective thermal responses of the control as well as the PCM-incorporated concrete, this section leverages the effective concrete properties as input to simulate the freeze-thaw response of concrete bridge deck under realistic ambient weather conditions. The following subsections elaborate on the geometry of the bridge deck, the consideration of the complex thermal interactions, and the obtained thermal responses from the bridge deck simulations.

The concrete structure considered herein is a box girder bridge, as shown in Fig. 6. The chosen geometry of the bridge deck is based on an existing bridge in Rhode Island, United States previously analyzed in [28]; however, it is important to note that the systematic approach proposed in this study can be applied to any general bridge deck.

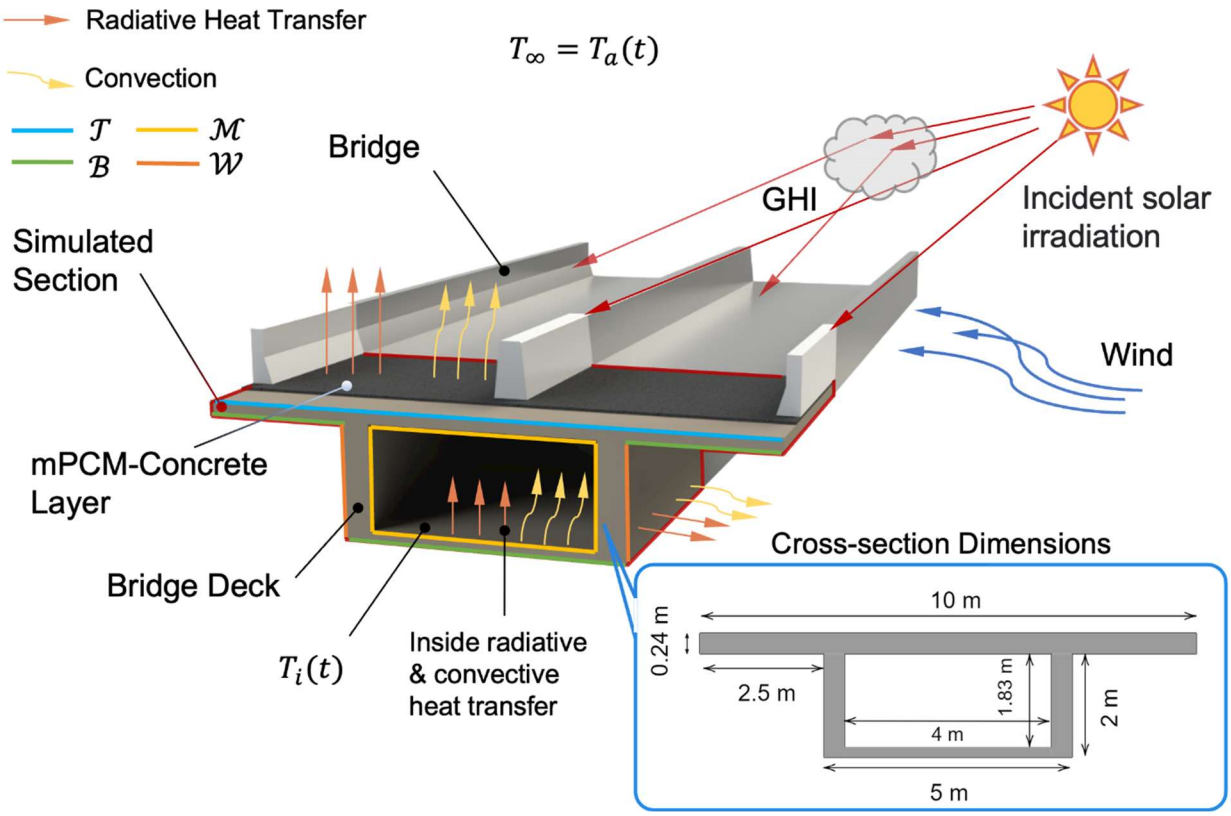

Fig. 6 A schematic of the bridge deck geometry and the thermal interactions between the bridge deck and the surroundings.

The width of the top surface of the bridge deck is 10 m, and the top slab has a thickness of 0.24 m. The box is of a rectangular shape, the height of the web is 2 m, and the bottom slab has a width of 5 m. The rectangle box's inner dimension has a height by the width of 1.83 m and 4 m. The protective layer is added on top of the bridge deck since most chemical and mechanical interactions happen on the top surface of the bridge. Also, an overlay on top of the bridge facilitates its implementation on existing bridges without altering the structural design and also reduces the potential cost by combining it into regular renovations of the bridges.

The boundary conditions and input properties for the bridge deck simulations

The key to realistic structural scale simulations is the proper determination of the interaction of the structure with the environment. The main contributive thermal interactions between the bridge and the environment involve [45–47]: (1) the solar radiation from the diurnal dynamics of the sun's motion, (2) the convective heat transfer on both the outer and inner surfaces of the bridge deck, and (3) the bridge irradiance to the ambient. For solar radiation, sinusoidal functions may be assumed to emulate diurnal solar radiation [47], and such radiation can be modeled by imposing a heat flux boundary condition with an effective heat flux using the global horizontal irradiance (GHI) [28]. Although solar irradiation affects the exterior surfaces exposed to sunlight, it is important to note that the interior surfaces of the box girder still experience convective heat transfer and radiative heat loss to the air inside the girder, caused by thermal radiation emitted from these surfaces. Similarly, the irradiation of the bridge can be modeled through the radiative heat transfer based on the Stefan-Boltzmann Law. Aside from the complex thermal interaction between the bridge deck and the environment, the dynamic variation of the environment also plays a vital role in the numerical simulations of concrete bridges [46]. Literature on the study of the freeze-thaw of PCM and PCM-incorporated concrete and thermal analysis of bridge deck often assumes sinusoidal temperature variation. Such simplification studies the freeze-thaw dynamics on a cycle-by-cycle basis which is easier to observe and characterize the magnitude and the lag in the temperature-time histories introduced by the latent heat effect from the PCM [41,42,47]. In reality, the temporal variations of the environment e.g., the temperature and the solar irradiance are irregular [48,49]. Hence, for longer timeframes, these irregularities in the ambient and the bridge deck temperature variations as well as the variations in the wind speed, and GHI become even more significant [50]. To ensure the fidelity of the simulations for real-world applications, real-time climate data is implemented in this study. The climate data is selected from the open-source national renewable energy laboratory (NREL) database [51]. We focus on the time-dependent ambient temperature, wind speed, and GHI values from December 15th, 2017, to February 14th, 2018, in Providence, RI, USA. This period is selected due to the higher occurrence of the FTCs solely based on the ambient temperature-time history illustrated in the histogram in Fig. 7 (a). The minimum and maximum values of the temperature-time histories are retained and linearly interpolated to emulate the half-day-based temperature cycles. The GHI-time history is converted into a triangular shape whose minimum values are the daily minimum values. The GHI value is kept at zero when no solar irradiance is present. On the other hand, the wind speed is converted to minimum-maximum reversals based on a 12-hour average due to the large variability, even within a day. The three environmental variations are shown in Fig. 7 (b). These field measurements serve as the boundary conditions during the numerical experiments.

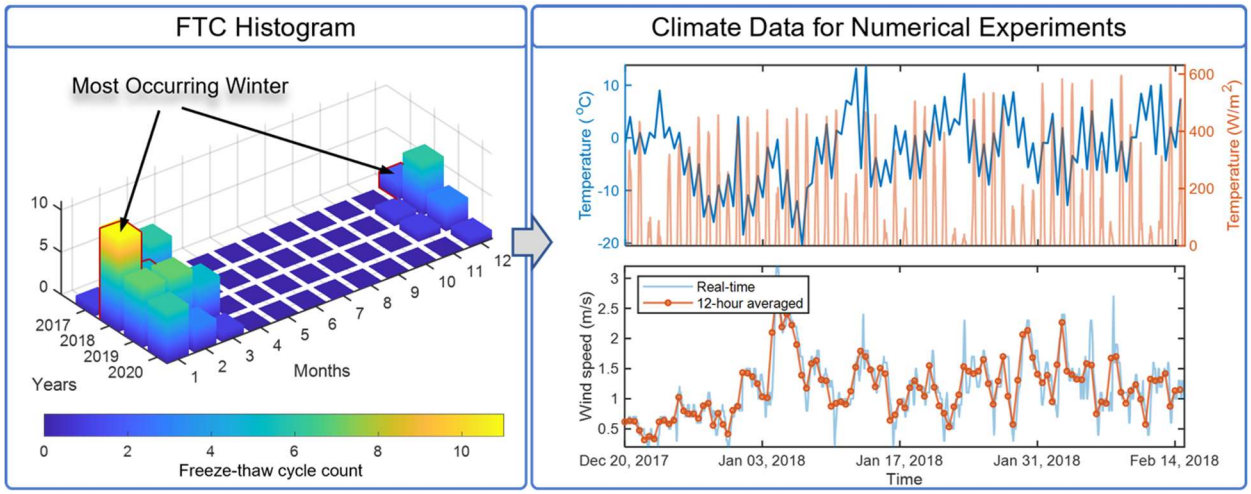

Fig. 7 A schematic of the main contributions of the thermal interaction between the bridge deck and the surrounding.

Table 5 summarizes the input parameters to define all the thermal interactions in the bridge deck. The time elapsed for computing at the macroscale level is, on average, 260 seconds.

Table 5. A summary of the physical constants used in the trial experiments

Interactions	**Irradiation**		**Convection**	**Radiation**	
Properties	GHI (W/m^2)	absorptivity	Emissivity (W/m^2)	Stefan-Boltzmann Constant ($W/(m^2 \cdot K^4)$)	Surface emissivity
Values	3.928	0.59	26	5.6697×10^{-9}	0.92

2.2.2 Neural-Network-Based Intelligent Design Space Modeling and Evaluation

While the previous section presented the numerical results for a case with a specific combination of input parameters primarily to showcase the effectiveness of the MPCMC protective layer as well as the versatility of the numerical model, this section varies the range of these input parameters so as to obtain the corresponding number of FTCs experienced by the bridge deck for a winter season to develop a consistent, complete, representative and unbiased large dataset for development of machine learning-based predictive model. Machine learning offers several advantages over multiscale numerical simulations for predicting freeze-thaw cycles, including higher computational efficiency, scalability, pattern recognition, robustness, continuous learning, and reduced reliance on domain expertise. These models can quickly process large datasets, identify complex relationships, and adapt to new information. By efficiently assisting materials designers, engineers, and decision-makers in adopting this technology, machine learning can contribute to user-friendly and reliable performance standard development, fostering large-scale implementation in practice. Despite these advantages, it is important to recognize that the multiscale simulation establishes a flexible and realistic simulation environment for one to explore the physical cause and effect between the considered design parameters of the protective overlay. However, finding the tuple of optimal design parameters using multiscale numerical simulations

is intractable due to the continuously defined parameter space and the high dimensionality of the parameter space, i.e., $\mathbb{R}^5$. Hence, the machine learning technique is deployed to approximate the underlying mapping between the parameters and the resultant number of freeze-thaw cycles (FTCs)**.** In this work, machine learning, particularly neural networks, leverages the labeled dataset generated by multiscale simulations to approximate the underlying relationship between design parameters and FTCs, creating a synergistic combination that makes design optimization tractable. The subsequent subsections outline the machine learning methodology, encompassing dataset generation, hyperparameter tuning, data interpretation techniques, and the presentation of both predictive and interpretative efficacy results in detail.

Dataset Preparation and tunning the neural network

The design parameters included for dataset preparation in this study involve the size effects of the MPCM capsules. They are the median size of the MPCM capsules (d_{PCM}) and the volume fraction of the MPCM (v_{PCM}) as a sand replacement. More importantly, the transition temperature (T_t) and the latent heat capacity (H) are included due to their contributions to altering the dynamic thermal responses of concretes. These design parameters have a wide range of design capabilities and customizability from commercially available databases. Moreover, at the bridge deck scale, the thickness of the protective layer (t_{ol}) is also included as a design parameter. Overall, these design parameters are selected based on the nature of the controllability during practical application. For engineering science, it provides insights into how the freeze-thaw dynamics are affected by designing such protective overlay. As for engineering practices, it practically guides engineers and practitioners to make cost-effective decisions during the anti-freeze-thaw designs. Thus, by varying the values of the design parameters a total of 4702 simulations are conducted and each case results in a temperature-time history like the ones shown in Fig. 7 from which the number of FTCs are counted.

As explained earlier, 4702 cases of numerical simulations are conducted, and their corresponding input-output pairs are used to train the FNN model. The hyperparameters to train the FNN are determined through a divide-and-conquer scheme with a training set size set to 80% of the total sample size. The training samples are further divided into training subsets (80%) and validation subsets (20%). The hyperparameter tuning involves the number of layers Nl, the number of hidden layer units per hidden layer Nn, the number of updates in the weights (i.e., epochs during training) Ne, the learning rate α, and the number of batches Nb. Whereas the activation function is set to rectified-linear type (i.e., the ReLU function), and the loss is set to the mean square error between the predicted FTC and the corresponding ground truth. The performance is evaluated based on the minimum validation error during training. Thus, the best-performing hyperparameter set is obtained as $Nl^* = 5$, $Nn^* = 70$, $Ne^* = 1000$, $Nb^* = 8$, and $\alpha^* = 0.0025$. The best model is saved with the initial weights and the final weights.

SHAP for Examining the Model Interpretability

According to the universal approximation theorem [52], the FNN can approximate any arbitrary nonlinear function with an arbitrarily small error. However, such high approximation accuracy comes with its lack of model interpretability. Thus, to quantify how the FNN model establishes the relationship between the design inputs and their corresponding output, the Shapley Additive

Explanation (SHAP) method is used here based on the cooperative game theory. SHAP provides an explanation of the model that characterizes the additive feature attribution of various inputs on the obtained outputs. To facilitate the evaluation of the Shapley values, the effect of removing a feature from the model is approximated by integrating over samples from the training data set. This relaxes the need to re-training the model for each held-out feature and, hence, reduces the computation complexity. As input features are involved, the marginal output value can be estimated after designating a particular set of input values, characterized by $\phi_i = E[f(z)|z_{1,\dots,i} = x_{1,\dots,i}]$. As a result, given a sample input feature $\{x_1, x_2, \dots, x_m\}$, the SHAP value can be obtained by adding the estimates up. After assigning each input feature, the values form a trajectory in the SHAP-feature plane, called the river flow of a given sample. Moreover, its projection onto the SHAP axis shows how each of the feature push or pull the value from the mean output estimate, which is called the force plot. Since the model evaluation involves many samples, the attribution of the features for each sample can be better illustrated in the form of a river flow plot. The river flow plots are bounded by some profile, indicated by the gray region in Fig. 8. SHAP explainer generally helps build a simple explanation model for complex machine learning models. It helps examine the model's capability in characterizing the input-output physical relation for interpretability. Recent applications of SHAP in cementitious composites can be found in [30,53,54].

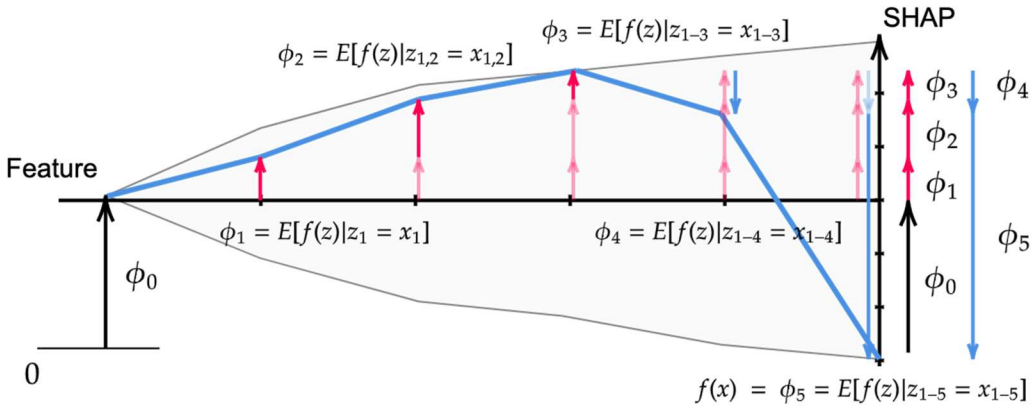

Fig. 8 SHAP river flow diagram which illustrates how the additive attribution assigns importance to each feature through the computation of ϕ_i for a given training sample (the blue curve).

Chapter 3: Results and Discussion

3.1 Experimental Results

Thermal Response of MPCM-mortars

Figures 9(a), (b) and **(c)** depict the representative heat flow-temperature curves for control mortar, PCM-10, and PCM-20 respectively, as determined by DSC. For ease of discussion, inset **Figures 9(a-1, b-1, and c-1)** show an enlarged version of the heat flow derivative (d(Q)/d(t)) curves for control and MPCM incorporated mortar samples focusing on the freezing of capillary pore water between the temperature ranges of -15 and -35 °C. The rapid cooling rate and confinement in DSC pans typically result in water freezing at approximately -20 to -24 °C [55], because of the supercooling effect where it tends to remain in a liquid state below its normal freezing point [56–58]. Additionally, cement's chemical composition, including ions in confined water, and the freezing dynamics of cement pores that shift from uniform to localized crystal growth, significantly impacts the freezing/melting temperature of water [59,60]. The freezing temperature peak of water in capillary pores measured in this study for control mortars (-25 °C) aligns well with findings reported by Bager and Sellevold [61]. It also needs to be noted here that the capillary pore water freezing peaks tend to shift to lower temperatures with increasing MPCM dosage. This can be explained from the fact that the progressive effect of MPCM releasing heat during the freezing process, making it more resistant to freeze at typical freezing temperatures. Inset **Figures 9(a-2, b-2, and c-2)** present the enlarged version of heat flow curves focusing on displaying the endothermic peak corresponding to the melting of ice during the heating cycle for control, PCM-10, and PCM-20 mortars respectively. Here, the endothermic melting curve indicates that the majority of ice melts close to 0 °C. The observed trend in these curves is consistent with DSC studies conducted on aged hardened cement paste (HCP) samples with a water/cement ratio of 0.4 [61–63]. From the figures, it can be clearly observed that as the MPCM dosage increases, there is a noticeable reduction in the melting enthalpy. The specific enthalpy values are provided in **Table 6**. Specifically, the enthalpy of fusion during melting for the control mortar was 2.07 J/g, while for PCM-20, it reduced to 0.13 J/g. This reduction is indicative of fewer ice crystals being formed, substantiating reduced ice melting during the heating cycle with MPCM inclusion.

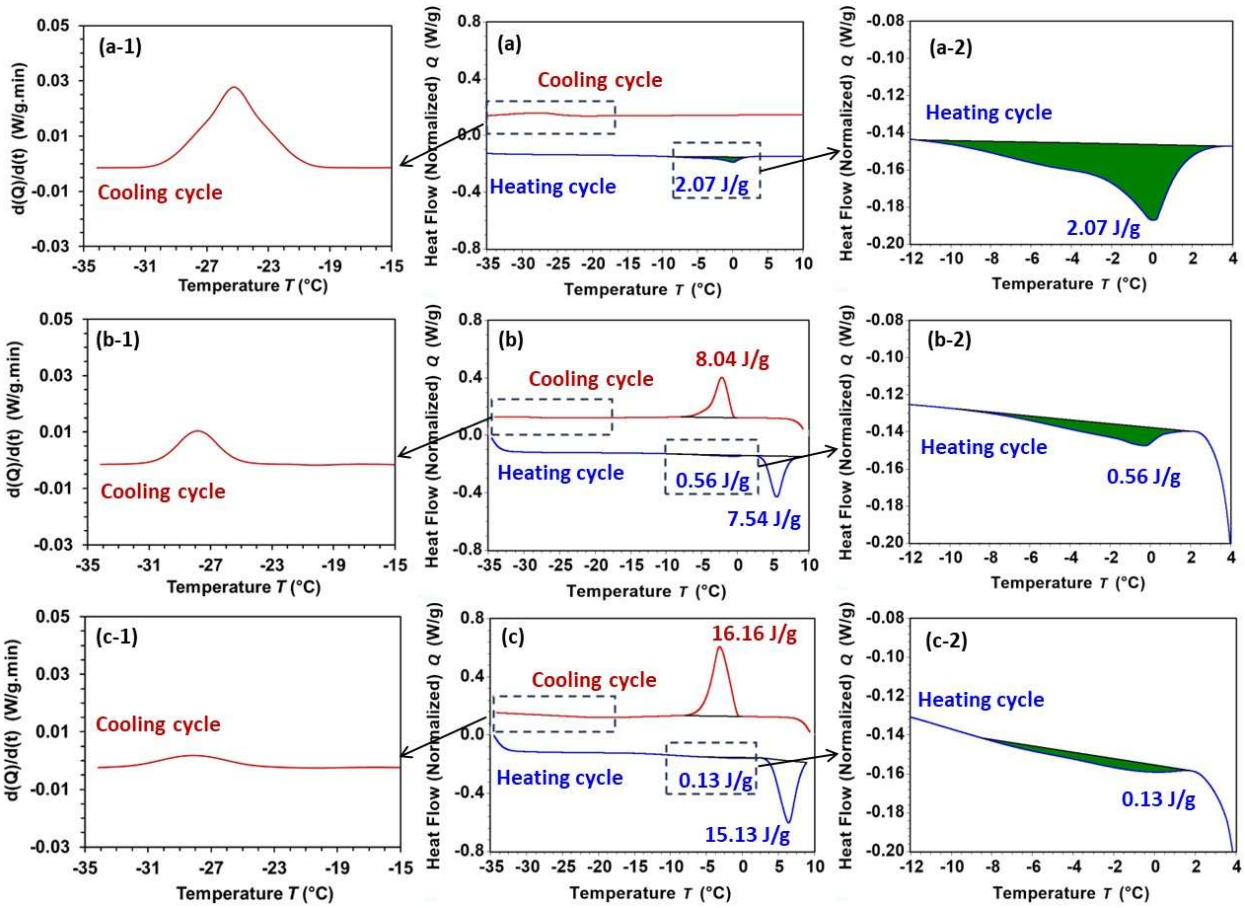

Figure 9. DSC heat flow vs. temperature profiles for (a) control, (b) PCM-10, and (c) PCM-20 mortar samples. The insets labeled (a-1), (b-1), and (c-1) provide detailed views of the derivative heat flow curves during cooling cycle focusing on displaying the capillary pore water freezing along the temperature range of -15 and -35 °C, while the insets (a-2), (b-2), and (c-2) show the detailed heat flow vs temperature plot during the heating cycle (4 to -12 °C) focusing on displaying the endothermic peak corresponding to melting of ice.

Table 6: Mean enthalpy of fusion values with standard deviations as indicators of ice content obtained during the ice-to-water phase transition across four replicate samples.

Samples	Enthalpy values during the ice melting process (J/g)
Control	2.07 ± 0.08
PCM-5	1.37 ± 0.06
PCM-10	0.56 ±0.03
PCM-15	0.27 ± 0.01
PCM-20	0.13 ±0.006

Figure 10 presents a comparative analysis of ice content in control and MPCM-integrated mortars. It showcases a clear inverse relationship between the MPCM concentration in the mortar and the amount of ice content: as the percentage of MPCM increases from 0% in the control sample to 20% in PCM-20, there is a corresponding decrease in ice formation within

the material. The Control mortar sample retains the most ice across the temperature spectrum, suggesting it is the most susceptible to freeze-thaw cycles. Whereas, the MPCM-infused mortars exhibit significantly lower ice content, demonstrating that MPCM inclusion is effective in mitigating ice accumulation, which is a critical factor for enhancing freeze-thaw durability.

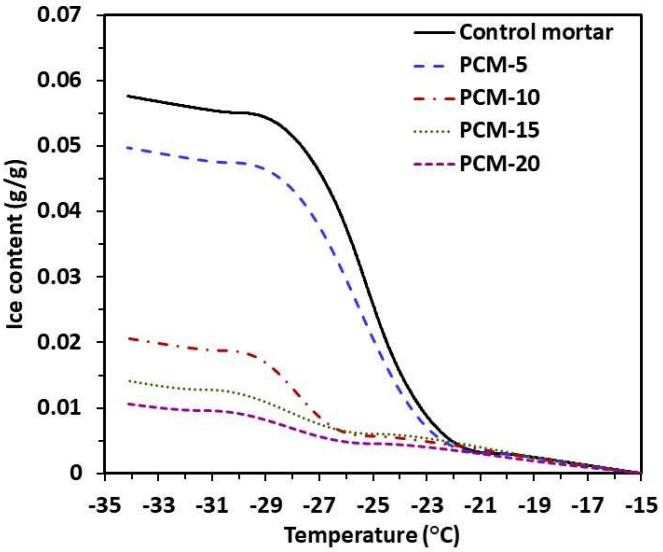

Figure 10. Ice content as a function of temperature in mortar samples. This figure compares the ice content in grams per gram of mortar for the control sample and samples with varying percentages of MPCM (PCM-5, PCM-10, PCM-15, and PCM-20). The figure highlights the decrease in ice content with the introduction of MPCM, indicating the effectiveness of MPCM in reducing freeze-thaw cycles in the mortar matrix.

To shed more light on the dynamics of the phase transformation of MPCMs, **Figure 11(a and b)** presents "conversion" (extent of a phase transition), and "conversion rate" (speed at which the phase transformation occurs) based on the DSC curves. These parameters provide insights into the kinetics of the phase transformations. The conversion progression from liquid (0) to solid-state (1) exhibits an identical shape for all the mortars. However, with increasing MPCM content from 5% - 20% there is a systematic shift of the conversion curves to the right, indicating a modulation in freezing behavior. Notably, the conversion curve for PCM-5 showcases a rapid rise in the temperature range of 0 to -2.5 °C, while the conversion progresses more gradually with increasing MPCM content. The rate at which these conversions occur provides insight into the freeze-thaw durability of mortar samples incorporating MPCM. The PCM-5 variant shows a rapid initial release of latent heat, indicative of a quicker conversion rate that diminishes over a shorter time span. As we increase the MPCM dosage from PCM-5 to PCM-20, there is a noticeable shift towards a more delayed and sustained release of heat, with PCM-20 offering the most extended duration of heat output, as depicted in **Figure 11(b)**. This progression suggests that higher MPCM dosages can effectively spread the heat release over a longer period, which aligns with the flatter, more prolonged peaks in the conversion rate graph. While the differences between PCM-10, PCM-15, and PCM-20 are less pronounced than when compared to PCM-5, the PCM-20's more consistent heat release within the 0 to -8 °C range implies the potential for improved mechanical performance under freeze-thaw conditions. It is important, however, to balance these benefits with the observed trade-off of

reduced initial strength at higher MPCM dosages. As such, this interplay between dosage, thermal behavior, and mechanical integrity underscores the need to identify an optimal MPCM concentration that maximizes durability without compromising the structural integrity of the mortar.

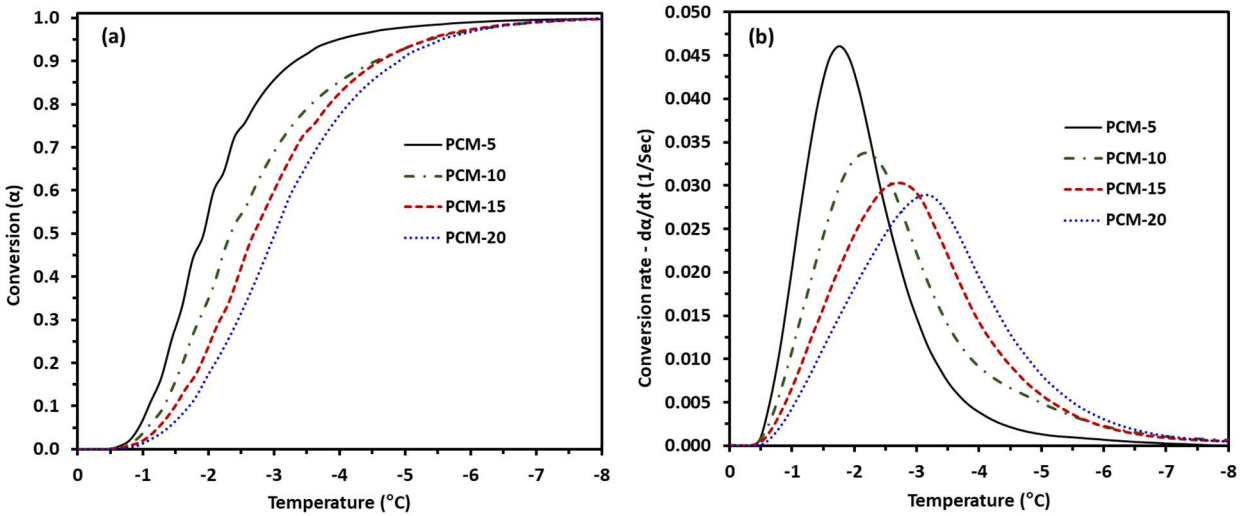

Figure 11. (a) Conversion and (b) conversion rate of MPCM-enhanced mortar samples during freezing. The conversion plot reveals a trend toward more sustained latent heat release with increased MPCM content. The conversion rate plot showcases a deceleration in heat release as MPCM dosage rises, with PCM-20 exhibiting the most gradual and extended release, indicative of enhanced freeze-thaw resistance.

Initial Mechanical Behavior of MPCM-incorporated Mortars

Figure 12 demonstrates the influence of MPCM dosage on the initial mechanical behavior of mortars before implementing freeze-thaw cycles. The compressive and flexural strength loss increases with increasing MPCM content, consistent with existing literature [4,64,65]. The reduction in strength observed with the incorporation of MPCM in cementitious composites is attributed to several interrelated factors. Primarily, the inclusion of MPCM microcapsules alters the volumetric composition of the mixture, by occupying a portion of the total volume. In our study, sand particles were partially replaced with MPCM. As sand serves as a load-bearing aggregate, its replacement with MPCM, which has lower strength and rigidity, results in a reduction in the material's ability to resist compressive loads. Additionally, the intrinsic properties of MPCM microcapsules, such as their lower strength and density compared to conventional aggregates, further contribute to strength reduction [66]. Another critical factor is the poor adhesion between MPCM and the cement paste, due to the microcapsules' smooth surface and polymeric nature, which limits mechanical interlocking. Studies like those by Pilehvar et al. [67] and Cui et al. [68] have demonstrated this weak interfacial adhesion. Furthermore, research has consistently shown that incorporating MPCM increases the overall porosity of the cementitious material [7,67,69,70]. This increase in porosity is a direct consequence of the microcapsules' presence, which introduces additional voids into the matrix. Higher porosity generally correlates with reduced strength and stiffness, as it diminishes the effective load-bearing area and facilitates crack initiation and propagation under stress.

As shown in **Figure 12(a)**, at lower MPCM content of 5%, the compressive and flexural strength loss is relatively small. The slight reduction can be attributed to the introduction of a small volume of MPCM. However, as the MPCM content increases from 5% to 10%, the impact on strength becomes more noticeable. This is due to the increase in replacement of sand with MPCM, which has lower strength and rigidity. As the MPCM content reaches 15%, the mortar undergoes further reductions in both compressive and flexural strength, as the weaker MPCM inclusions replace a more substantial portion of the solid structure, diminishing the material's ability to resist mechanical loads. At 20% MPCM dosage level, this reduction in compressive and flexural strength increases from 19% to 35% and 22% to 37% respectively, which demonstrate that this inclusion level has slightly disrupted the continuity of the matrix, due to poor adhesion and week bonding of MPCM with matrix. This reduction in strength due to the inclusion of MPCM has been similarly reported in other studies [68,71], highlighting the mechanical trade-offs associated with incorporating MPCM into cementitious materials.

This trend is also reflected in RDME **(Figure 12(b))**, where a reduction of 6%, 11%, 20%, and 35% is observed at 5%, 10%, 15%, and 20% volume replacements, respectively. This reduction is directly linked to the more porous structure caused by MPCM inclusion. While the reduction in compressive strength may be seen as a negative for structural applications, the decrease in elastic modulus offers potential benefits in certain conditions, particularly in crack control. A lower elastic modulus reduces the accumulation of stress, especially in systems subjected to restrained deformation - a scenario common in concrete composite subjected to thermal or moisture fluctuations [72,73]. This behavior is advantageous in controlling cracking by allowing the material to deform more before significant stress buildup occurs. A prior investigation by Falzone et al. [74] has demonstrated a similar reduction in the stiffness of cementitious composites, due to the inclusion of MPCM. The relationship between increased porosity and diminished mechanical performance highlights the importance of meso-structural integrity in maintaining the strength and stiffness of MPCM-incorporated mortars.

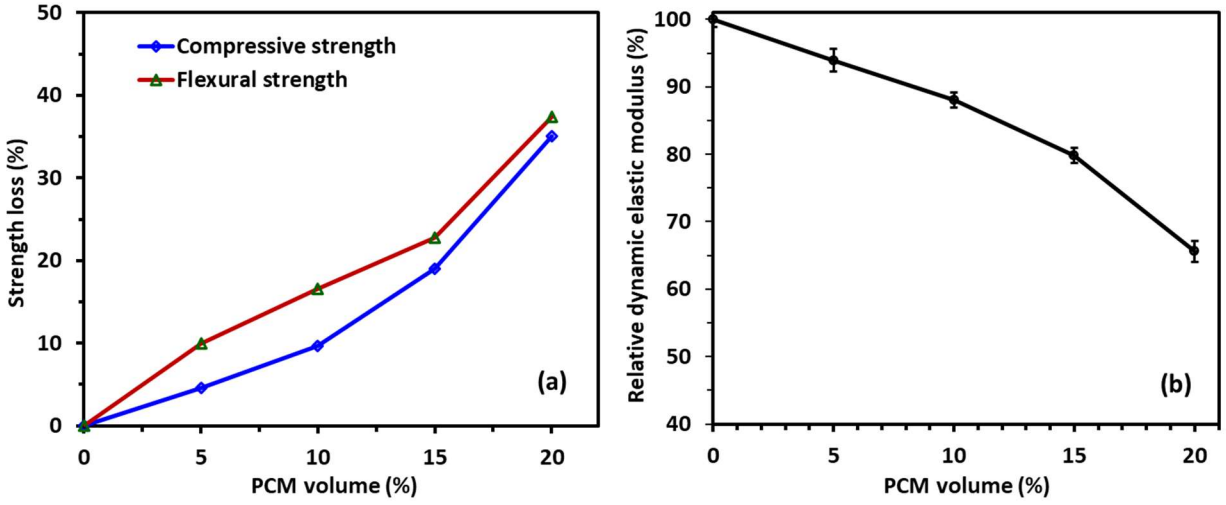

Figure 12. Impact of MPCM dosage on the initial mechanical properties of cementitious composites: (a) percentage loss in compressive and flexural strength and (b) relative dynamic elastic modulus with varying MPCM dosage. The strength loss results indicate a proportional

decrease in mechanical strength with higher MPCM content whereas the relative dynamic elastic modulus response shows a notable decline as the MPCM dosage is increased.

Overall, the incorporation of MPCM into cementitious materials leads to slight reduction in strength and stiffness due to a combination of volumetric replacement, low intrinsic strength and density of the microcapsules, weak adhesion between MPCM and cement, and increased porosity. Nevertheless, even with this reduction, the resulting strength remains sufficient for structural applications, the lowest recorded compressive and flexural strength in concrete containing 20% MPCM was 35 MPa and 5.7 MPa, respectively. The integration of MPCM in cementitious composites provides a promising pathway for enhancing thermal performance without severely compromising mechanical properties. This trade-off between reduced strength and improved thermal regulation highlights the need for careful consideration of the balance between structural performance and energy efficiency, that is critical for the development of sustainable and resilient construction materials.

Freeze – thaw Performance of Mortars Incorporating MPCM

Figure 13(a) quantifies the compressive strength of mortars with different MPCM contents over varying numbers of freeze-thaw cycles, while **Figure 13(b)** tracks the relative percentage of strength loss with respect to the initial strength due to the implementation of freeze-thaw cycles. Together, they reveal the influence of MPCMs on mortar durability. In **Figure 13(a)**, the compressive strength of all mortars decreases with an increasing number of freeze-thaw cycles; however, the control mortar starts with the highest strength but also shows significant degradation over time. On the other hand, while MPCM-containing mortars begin with lower initial strengths, they exhibit a trend of improved freeze-thaw resistance compared to the control, evident from the less pronounced strength loss in **Figure 13(b)**. Specifically, mortars with higher MPCM content (PCM-20), demonstrate the greatest endurance, indicating a beneficial trade-off between initial compressive strength and long-term durability. After enduring 324 freeze-thaw cycles, the control mortar lost approximately 60% of its initial compressive strength, a significant reduction reflecting its vulnerability to such environmental stressors. Conversely, the mortar containing 10% MPCM demonstrates enhanced resilience, with a comparatively lower strength loss of about 25% under the same conditions. The trend of increased durability with higher MPCM content is further exemplified by the mortar with 20% MPCM, which exhibits the most robust performance, retaining a greater portion of its compressive strength and showing only about a 7% reduction after the same number of freeze-thaw cycles. This data quantitatively underscores the potential of MPCMs in improving the freeze-thaw durability of mortars without overly compromising their initial compressive strength.

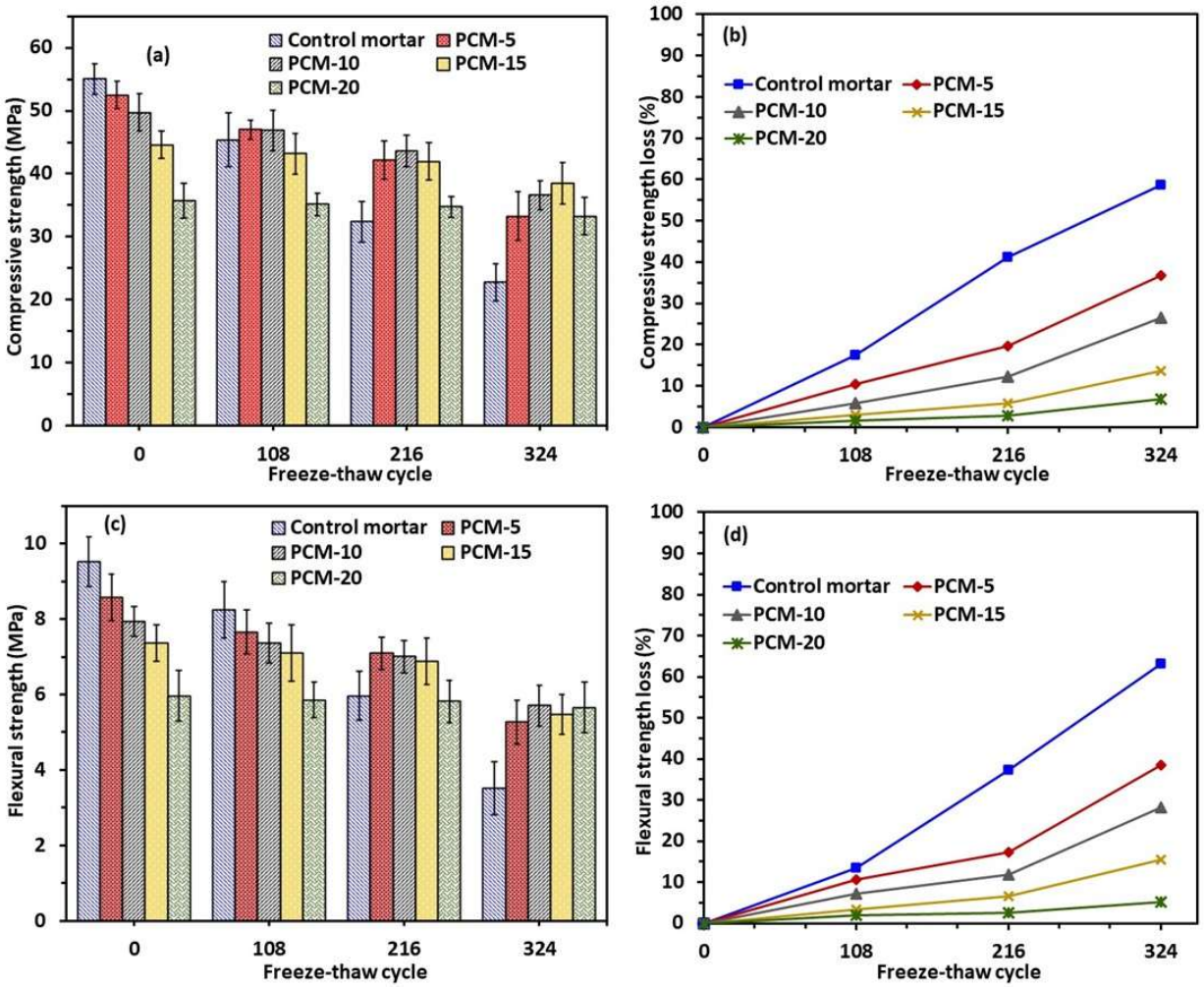

Figure 13. Comparative mechanical degradation of control mortar and MPCM incorporated mortars under progressive freeze-thaw cycles: (a) compressive strength, (b) relative compressive strength loss, (c) flexural strength, and (d) relative flexural strength loss with increasing number of freeze-thaw cycles.

The flexural strength showcased in **Figures 13(c) and (d)** reflects a similar trend to that observed in compressive strength. After 324 freeze-thaw cycles, the control mortar exhibits a substantial reduction in flexural strength, dropping by more than 60%. After the same number of freeze-thaw cycles, mortar with 10% MPCM sustains a markedly lower flexural strength loss of around 25%, while mortar with 20% MPCM exhibits outstanding durability, with a minimal flexural strength reduction of just about 6%. These figures point to a clear correlation between higher MPCM content and a decreased rate of strength degradation, further corroborating MPCM's role in fortifying mortar against freeze-thaw-induced damage. In line with the observations in compressive and flexural strength evolution with increasing freeze-thaw cycles, the RDME of the mortar samples also exhibits a dependency on MPCM content and freeze-thaw exposure, as shown in **Figure 14**. The modulus reduces as the freeze-thaw cycles progress, yet this reduction is notably less severe in MPCM-incorporated mortars. At 216 freeze-thaw cycles, the RDME of the control mortar falls below 60%, suggesting the loss of frost resistance [14,75]. For the same number of freeze-thaw cycles, the RDME for MPCM integrated mortars does not fall below 60%, suggesting

excellent resistance to frost cycles. As the number of cycles increases to 324, the control mortar suffers even more significant drop in modulus, whereas mortars with MPCM retain a greater portion of their original modulus, with PCM-5 experiencing the greatest decrease (falling slightly below 60%) and PCM-20 showing the smallest decrease in RDME, suggesting enhanced durability and an improved ability to withstand the freeze-thaw conditions.

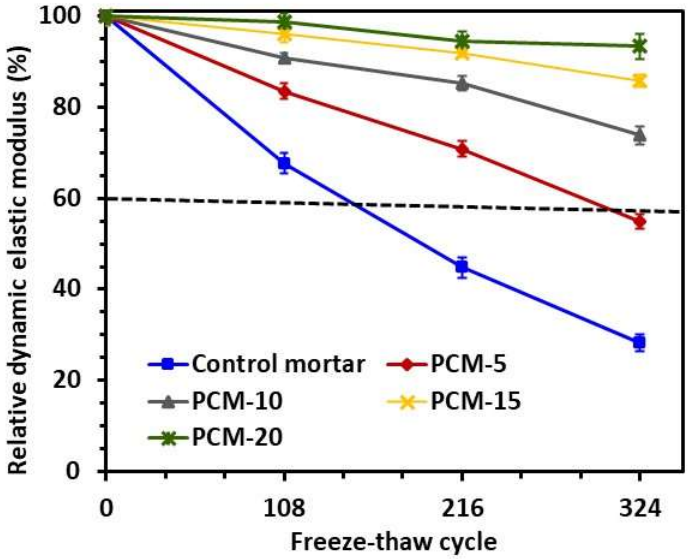

Figure 14. Comparative analysis of relative dynamic modulus of elastic (RDME) across freeze-thaw cycles for control and MPCM-infused mortars. The figure demonstrates the impact of MPCM inclusion on the frost resistance of mortar, with higher MPCM percentages correlating with enhanced durability and consistent modulus retention.

To complement the strength and RDME evaluations and to visually assess the damage states for a more comprehensive analysis, **Figure 15** illustrates the apparent visible changes in both control and MPCM-incorporated mortars following 324 freeze-thaw cycles, compared to the samples not exposed to freeze-thaw cycles. MPCM-integrated mortar samples exhibit no substantial visible damage. However, presents minor weathering of materials on the surface indicated within the red dotted lines in **Figure 15**. In contrast, control mortar samples display significant weathering, as well as upheaval at surfaces, corners, and edges. The primary mechanism behind the degradation of cementitious materials during freeze-thaw cycles is the expansion of water. As the temperature drops, the water in the pores undergoes freezing, resulting in a volume expansion of approximately 9% [76–78]. This expansion generates hydraulic pressure within the material. When the pressure exceeds the tensile strength, microcracks develop, and with repeated freeze-thaw cycles, these microcracks expand, causing intense degradation [79–81]. Consequently, the strength of the samples decreases rapidly for the control mortar. In contrast, integrating MPCM with rationally low transition temperatures significantly improved the frost resistance of mortar, preserving its integrity and overall performance. This visual evidence supports and reaffirms the strength and RDME results, indicating that the enhanced durability observed is not only measurable but also visibly discernible. The enhancement in frost resistance is attributed to the favorable impact of MPCM, which releases latent heat, as evidenced in DSC scans, causing a delay in the freezing peak and ice nucleation within the pores. This release of heat serves as a thermal buffer, restricting ice formation and mitigating the harmful consequences of freezing, especially frost heave damage.

The impact becomes increasingly evident as the quantity of MPCM rises. Additionally, finer pore structures are known to be more vulnerable to frost damage due to increased crystallization pressures in smaller pores [82,83]. However, the inclusion of MPCM leads to increased porosity, introducing more voids. These voids function as expansion reservoirs for freezing water, strengthening frost resistance, and alleviating stress induced by frost [67,84]. To investigate this phenomenon further, the forthcoming section presents an extensive analysis of the evolution of pore structure in mortars with and without MPCM integration across different freeze-thaw cycles, utilizing X-ray tomography for precise visualization and assessment.

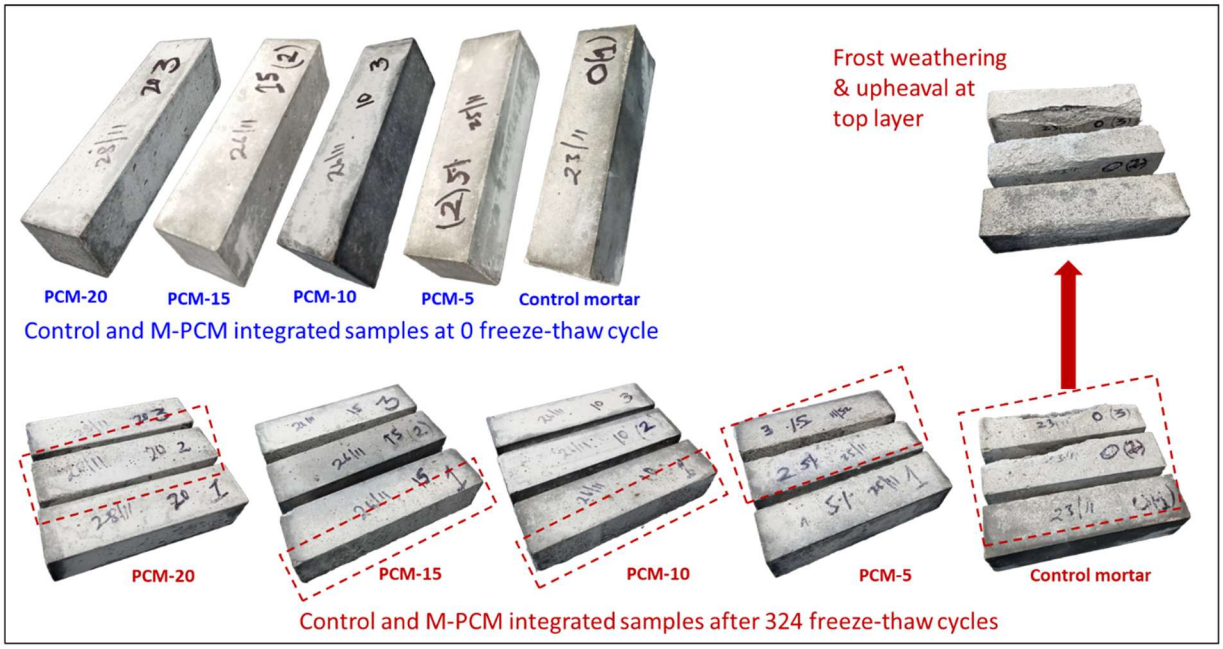

Figure 15. Visual comparison of control and MPCM-integrated mortar samples before and after exposure to freeze-thaw cycles. The top images display the samples with varying concentrations of MPCM prior to freeze-thaw cycles, and the bottom images showcase the same samples after enduring 324 freeze-thaw cycles. Significant frost weathering and surface upheaval can be observed in the control sample, while the MPCM-integrated mortars display markedly less damage, highlighting their enhanced resistance to freeze-thaw conditions.

X-Ray micro-Tomography Analysis of Freeze-thaw-induced Mortar Samples

Figure 16 depicts 2D cross-section XRT images illustrating the progressive damage in control and MPCM-incorporated mortars at the same region of interest. This region features the center of the target volume cylinder with a diameter of 3.93 mm and a height of 4.03 mm. **Figures 16(a1-a3)** depict the control mortar without MPCM addition whereas **Figures 16(b1-b3)** present visual results for the mortar containing 10% MPCM (PCM-10) and **Figures 16(c1-c3)** show the results for mortars with 20% MPCM (PCM-20). In the first set of **Figures 16(a1-a3)**, we observe the control mortar at various stages: prior to freeze-thaw cycling (a-1), after 216 cycles (a-2), and following 324 cycles (a-3). Initially, the control mortar (a1) presents a dense structure. However, after 216 cycles (a2), there is a visible increase in porosity and microcrack formation, which becomes more pronounced by the end of 324 cycles (a3) where a significant number of interfacial cracks are observed between the cement paste and aggregate, indicating substantial structural

degradation due to the freeze-thaw effect. The interfacial transition zone (ITZ) is the primary region where damage and cracks occur, owing to the distinct material characteristics during the cement hydration process [85,86]. The poor frost resistance of the control mortar results in noticeable interfacial cracks caused by freeze-thaw damage. Occasionally, cracks extended through both the cement matrix and aggregates and pre-existing cracks were observed progressing during the freeze-thaw cycles, as shown in **Figure 16(a2 and a3)**.

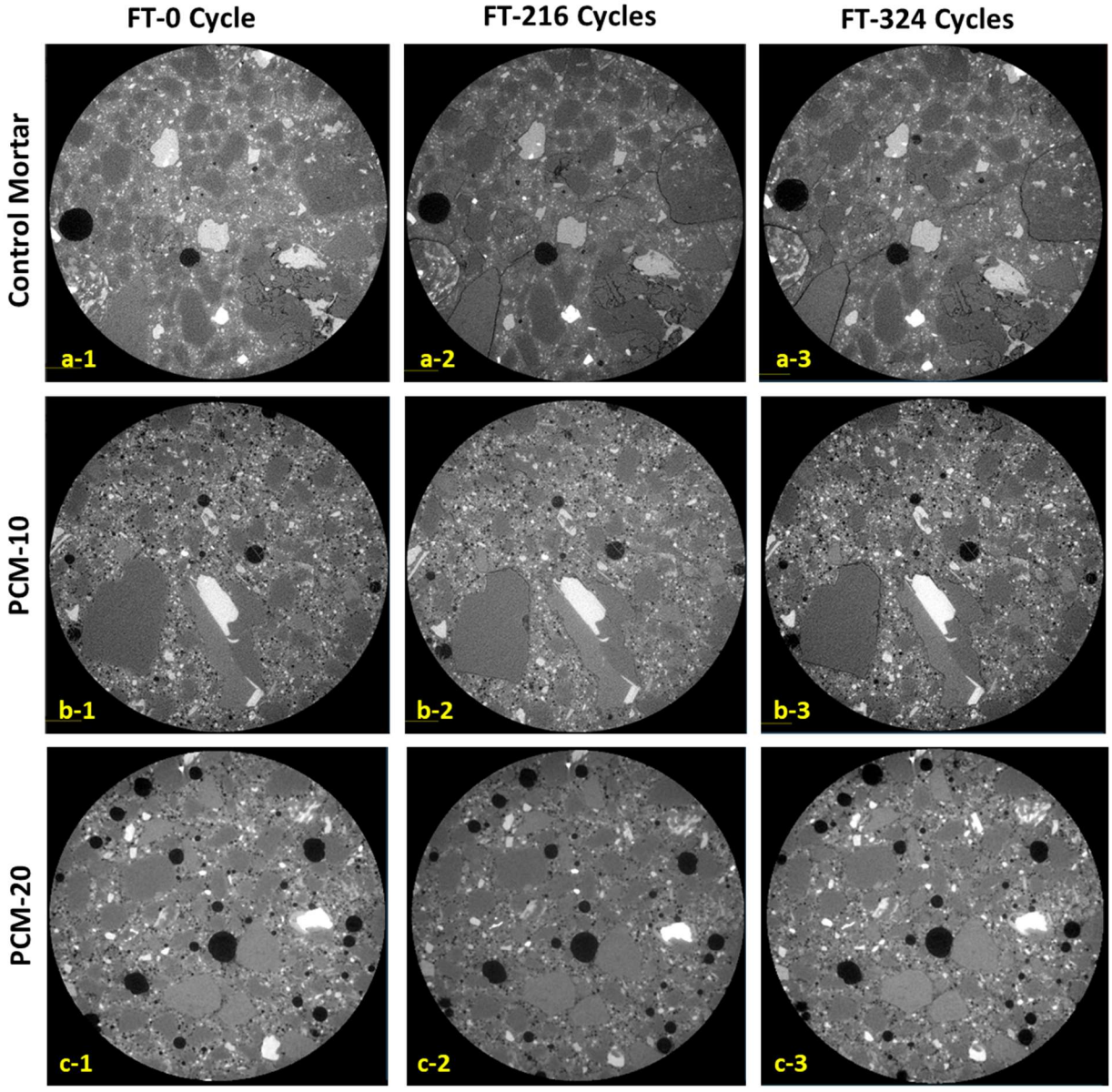

Figure 16. 2D images of mortar samples illustrating progressive freeze-thaw damage under X-ray tomography after 0, 216, and 324 freeze-thaw cycles. Figures a1, b1, and c1 showcase the initial state of control, PCM-10, and PCM-20 mortars respectively, without any freeze-thaw cycles. Images a2, b2, and c2 display the corresponding samples after 216 freeze-thaw cycles, and images a3, b3, and c3 illustrate the samples following 324 cycles, highlighting

the superior resistance to freeze-thaw induced micro-cracking in MPCM-incorporated mortars as compared to the control mortar.

Figures 16(b1-b3) showcase the XRT image of the PCM-10 sample across the same freeze-thaw intervals. The initial state (b1) also displays a relatively dense structure, yet with slightly more initial porosity compared to the control mortar, owing to the MPCM inclusion. After undergoing freeze-thaw cycles, it is clear that the PCM-10 samples (b2 and b3) exhibit some damage, but it is less severe than in the control samples. This suggests that the presence of MPCM at this concentration acts to mitigate the freeze-thaw damage. Finally, **Figures 16(c1-c3)** display the PCM-20 samples, where the initial porosity (c1) increases compared to the control mortar, similar to that of PCM-10. After 216 cycles (c2) and 324 cycles (c3), these samples show the smallest increase in porosity and the least crack propagation among the three groups. This indicates that a higher MPCM content significantly enhances the freeze-thaw resistance of the mortar. The MPCM's thermoregulatory function likely plays a key role in reducing the freeze-thaw damage, thus preserving the structural integrity of the mortar.

In summary, our initial examination reveals that mortar samples containing MPCM exhibit an increase in porosity, attributed to the higher volume of MPCM incorporated into the mortar mix. As discussed earlier in the study, this increase in porosity arises primarily from the physical presence of MPCM microcapsules, which replace a portion of the aggregate, leading to the creation of additional voids within the mortar matrix. While this elevated porosity may initially compromise the compressive and flexural strength of the mortar due to the reduction in effective load-bearing area [68,87], these voids serve a critical and strategic purpose in mitigating freeze-thaw damage. The increased porosity allows for the accommodation of the volumetric expansion of water when it transitions to ice during freeze-thaw cycles. When water freezes, it expands by approximately 9%, exerting significant tensile stress on the surrounding mortar matrix. Previous research has demonstrated that materials with higher porosity can better absorb this expansion, effectively relieving internal stresses and reducing the likelihood of crack formation [88,89].

Moreover, the thermoregulatory function of MPCM plays a pivotal role in reducing freeze-thaw damage and enhancing the durability of mortar. MPCMs absorb and release latent heat during phase transitions, effectively moderating the temperature fluctuations within the mortar matrix. The thermoregulation afforded by MPCM can delay the onset of freezing conditions, allowing the mortar to remain within a more favorable temperature range [69]. At 5% MPCM content, the thermal buffering effect is moderate, as a limited volume of MPCM is available to store and release heat. As the MPCM content reaches 10-20%, the thermal buffering effect becomes more substantial. The increased MPCM volume enhances the material's ability to moderate temperature fluctuations, reducing the formation of ice as shown in **Figure 10**. Furthermore, the enhanced thermal stability provided by MPCM can reduce the frequency and severity of freeze-thaw cycles that the mortar is subjected to, ultimately preserving the structural integrity of the material. This property is critical in environments subject to cyclic freezing and thawing, as it mitigates the thermal shock that can occur when temperature variations lead to rapid expansion and contraction of water/ice in mortar matrix. Research by Nayak et al. [90] and Li et al. [91] supports this notion, indicating that the incorporation of MPCM into concrete can significantly decrease the temperature gradient within the material, thereby enhancing its resistance to thermal stresses.

While the 2D meso-structures obtained from XRT support the hypothesis that a higher inclusion rate of MPCM can considerably improve the mortar's durability and extend its service life in environments subject to freezing and thawing conditions, it is important to acknowledge that analyzing just 2D regions of interest might not paint the full picture. Therefore, to fully evaluate internal damage and deterioration, 3D reconstructed volumes derived from multiple 2D slices were examined, allowing for a more detailed and quantifiable analysis of the material's integrity when subjected to freeze-thaw cycles.

Figure 17 presents a 3D visual analysis of crack and pore development in control mortar subjected to different stages of freeze-thaw cycles. The leftmost column (a1-c1) shows the 3D greyscale images of the control mortar sample, providing a raw visual context of the internal structure at 0 (a1), 216 (b1), and 324 (c1) cycles. The second column (a2-c2) offers a closer look by highlighting the segmented pores and cracks within the greyscale images. This segmentation process makes it easier to observe the spatial distribution of the voids and cracks with respect to other solid phases and interfaces. Notably, as the number of freeze-thaw cycles increases from figures a-2 to b-2 to c-2, there is a clear expansion of voids and the emergence of cracks, particularly at the aggregate-matrix interfaces due to the inherent weakness of the ITZ [86]. This pattern of degradation continues with even smaller pre-existing pores becoming more pronounced. In the third column (a3-c3), the segmented pores and cracks are shown along with the corresponding aspect ratios of the pores for 3D visualization. This visualization aids in quantifying the porosity of the mortar and provides a detailed three-dimensional view of the evolution of pores and cracks affected by the freeze-thaw cycles. The 3D images in figures a-3 through c-3 offer a clearer visualization of the progressive damage, highlighting a significant amplification of pore spaces and crack propagation as the cycle count rises. Particularly after 324 cycles, the increase in porosity and cracking is much more substantial compared to the pre-freeze-thaw state. To elucidate the aspect of freeze-thaw-induced crack progression further, figures b-4 and c-4 meticulously highlight the freeze-thaw-induced segmented cracks, isolated from the pores to emphasize the initiation and propagation of these cracks over time. The figures clearly show a significant proliferation of freeze-thaw-induced cracks, many of which emerge around the ITZ regions. This observation supports the theory that the ITZ serves as a focal point for damage during freeze-thaw conditions due to its weaker mechanical properties [86].

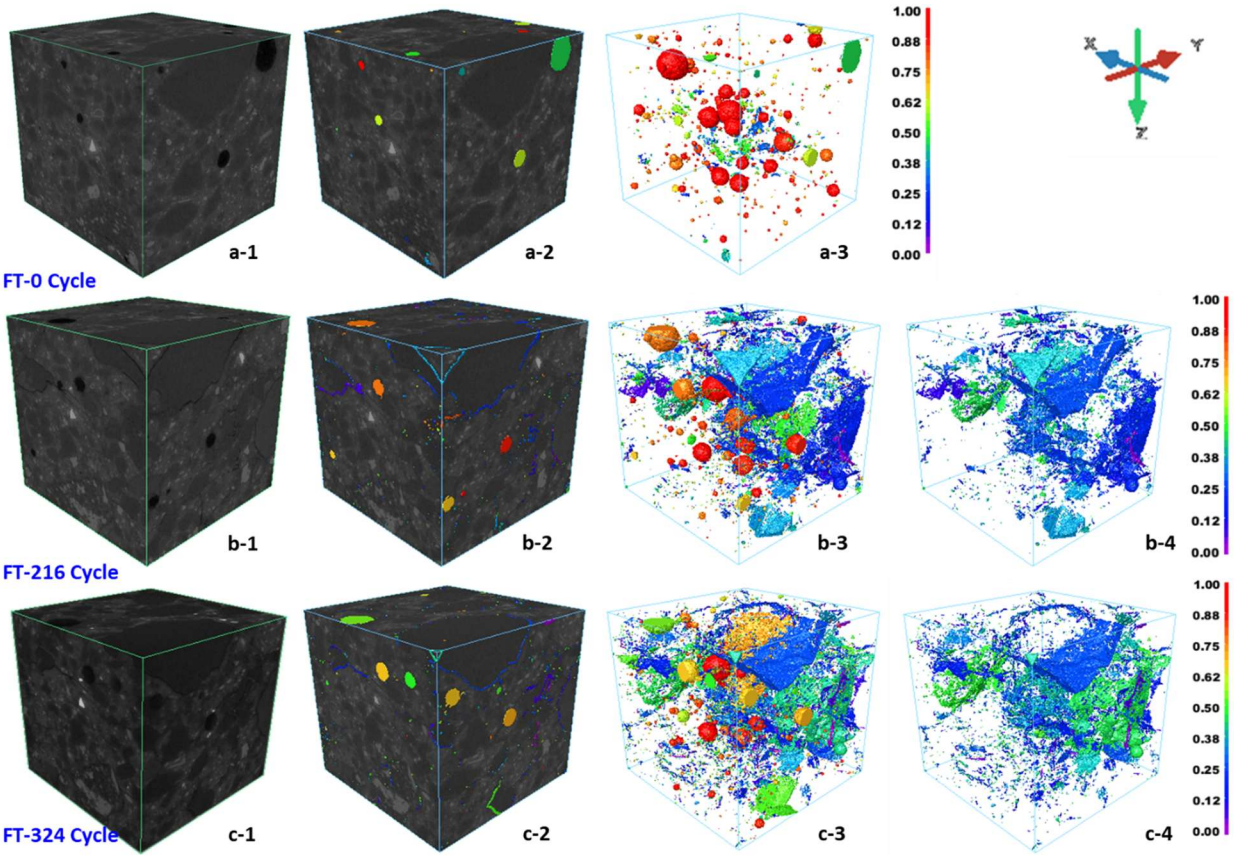

Figure 17. Progressive freeze-thaw damage in control mortar visualized in 3D. Greyscale images showing: (a-1) the initial meso-structure before any cycles, (b-1) after 216 cycles, and (c-1) after 324 cycles. Corresponding, segmented visualization of pores and cracks is presented in a-2, b-2, and c-2 on greyscale images, illustrating the freeze-thaw-induced damage progression around the solid meso-structural features. 3D views of the pores and damage evolution without the greyscale solid phases are provided in a-3, b-3, and c-3, while b-4 and c-4 exclusively detail the significant growth of freeze-thaw induced cracks through the cycles, particularly highlighting the ITZ as a critical zone of damage.

Overall, the analysis for the control mortar as presented in **Figure 17** reveals a progressive increase in the volume of pores and cracks increasing with the advancing number of freeze-thaw cycles. This aligns with the deterioration of mechanical properties reported earlier, illustrating a tangible link between the observed physical damage within the mortar's meso-structure and its declining mechanical integrity. Similar to **Figure 17**, **Figure 18** illustrates the effects of freeze-thaw cycles on the pore structure of PCM-10 mortar, as captured by 3D XRT. The greyscale images a-1, b-1, and c-1 provide baseline visuals of the meso-structure before any cycles, after 216 cycles, and after 324 cycles, respectively. The segmented images a-2, b-2, and c-2 show the progression of freeze-thaw-induced damage and highlight the PCM-10's role in reducing the development of pores and cracks within the mortar matrix. The 3D images a-3, b-3, and c-3 offer clear evidence of the material's increased resistance to damage compared to the control, showing a less extensive network of pores and cracks. Finally, the segmented crack images b-4 and c-4 exhibit only minor crack formation even after numerous cycles, underscoring the effectiveness of PCM-10 in preserving structural integrity under freeze-thaw cycles.

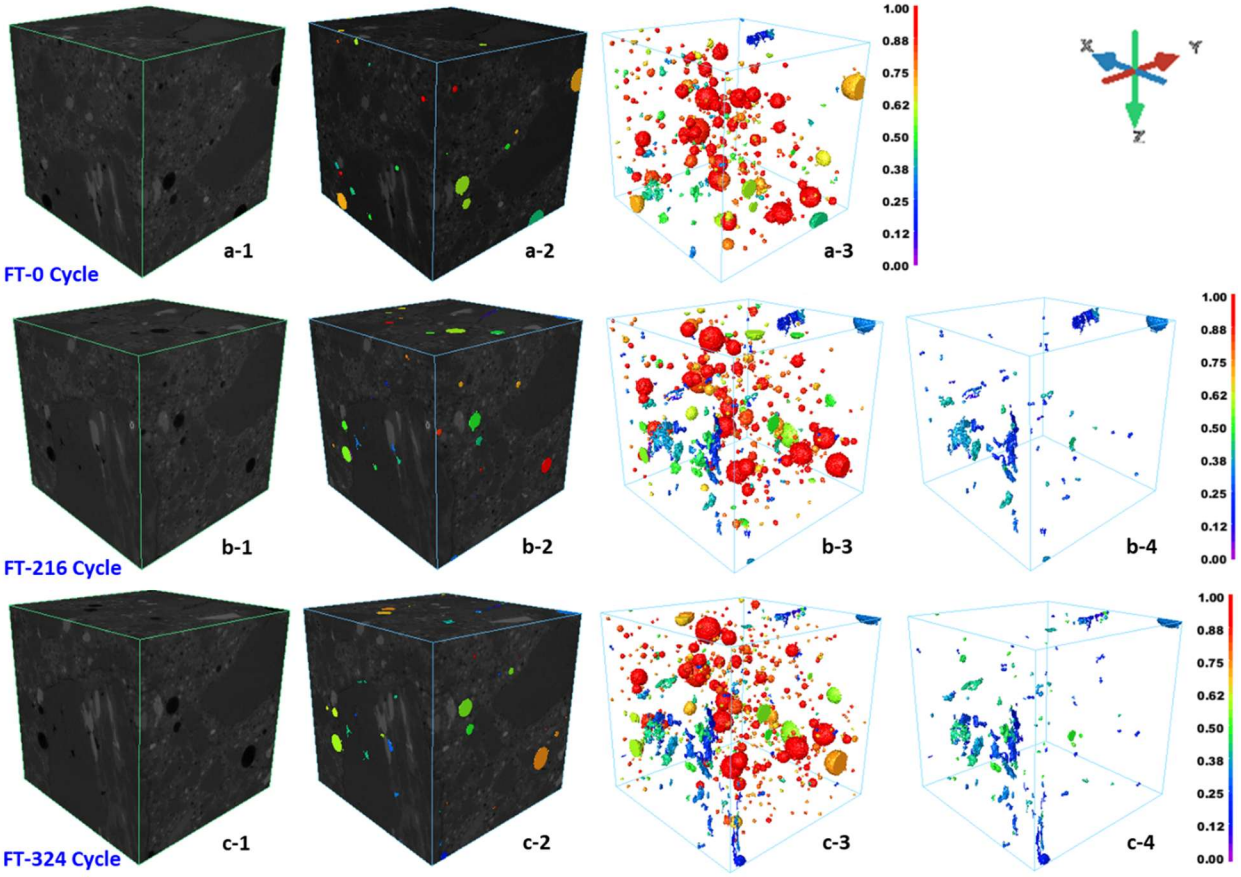

Figure 18. Visualization of reduced freeze-thaw damage in PCM-10 mortar in 3D. The greyscale images showing the PCM-10 mortar's meso-structure at (a-1) zero, (b-1) after 216 cycles, and (c-1) following 324 cycles, respectively. Compared to the control, these images, along with their segmented counterparts a-2, b-2, and c-2, reveal a less severe development of pores and cracks, suggesting the mitigating effects of MPCM against freeze-thaw damage. The 3D visualizations of pores and damage progression, depicted in a-3, b-3, and c-3, further demonstrate the mortar's resilience, with a noticeably lower extent of cracking and porosity expansion. Images b-4 and c-4, which isolate the freeze-thaw-induced cracks, confirm the limited progression of structural deterioration over time, evidencing the MPCM's role in enhancing the durability of the mortar against freeze-thaw cycles.

Figure 19 depicts the effects of incorporating 20% MPCM in mortar (PCM-20) subjected to freeze-thaw cycles, using 3D X-ray tomography for visualization. Greyscale images a-1, b-1, and c-1 display the mortar's initial meso-structure and its condition after 216 and 324 freeze-thaw cycles, respectively. The presence of PCM-20 further reduces the appearance of freeze-thaw damage compared to PCM-10, as seen in the segmented images a-2, b-2, and c-2. These images show the spatial configuration of pores and cracks, with PCM-20 demonstrating even greater resistance to crack propagation and pore enlargement. In the focused 3D representations, a-3, b-3, and c-3, the reduction in damage is even more evident, with fewer and less significant pores and cracks. No cracking was observed for up to 216 freeze-thaw cycles. The segmented crack images c-4 after 324 freeze-thaw cycles confirm the minimal

progression of cracking, highlighting PCM-20's superior performance in mitigating the detrimental effects of freeze-thaw cycles.

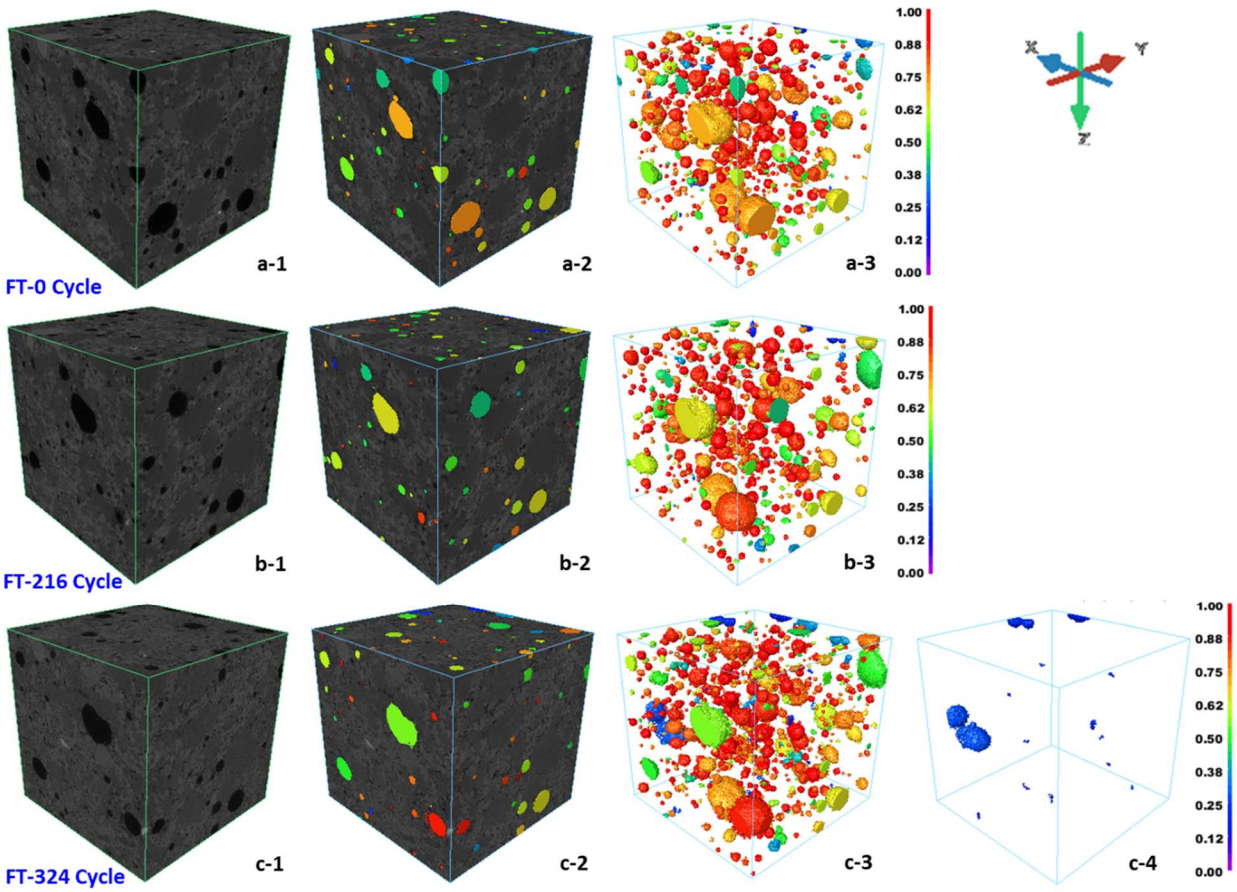

Figure 19. The durability of PCM-20 mortar against freeze-thaw cycles illustrated through 3D XRT images. Greyscale images represent: (a-1) the intact meso-structure before freeze-thaw cycles, (b-1) after 216 cycles, and (c-1) following 324 cycles, respectively. Segmented visualizations a-2, b-2, and c-2 show the pores and cracks in the greyscale image demonstrating minimal change of pores and crack volumes after freeze-thaw cycles. The 3D renderings a-3, b-3, and c-3 demonstrate the 3D pore structure evolution. Figure c-4 displays the freeze-thaw-induced cracks isolated from the pore structure inherently present in the meso-structure where minimal crack development was observed. No such image is provided here for 216 cycles as no crack was detected after image segmentation. The overarching outcome indicates that PCM-20 offers robust protection, effectively preserving the mortar's meso-structure even after extensive freeze-thaw exposure.

In concluding the comparative analysis between control, PCM-10, and PCM-20 mortar samples across varying freeze-thaw cycles, it is evident that the incorporation of MPCMs significantly influences the resistance of mortar to freeze-thaw cycles. The control samples, with no MPCM, exhibit a progressive increase in both pore size and crack formation, indicative of the severe structural degradation inherent to traditional mortar under such cyclic conditions. PCM-10 samples show marked improvement, with reduced porosity and fewer freeze-thaw-induced cracks, affirming MPCM's role in enhancing durability. However, PCM-20 samples

stand out with even more impressive results; they display minimal changes in porosity and scant crack development, after 324 freeze-thaw cycles. This suggests that PCM-20 not only mitigates the immediate effects of freeze-thaw conditions but may also offer long-term improvements to the mortar's overall lifespan and structural integrity, making it a potentially transformative addition to cementitious composites in frost-prone regions.

Figure 20(a) presents the quantification of pore and crack volumes obtained from image analysis of the XRT images before and after exposure to freeze-thaw cycles. The introduction of MPCM leads to increased porosity in mortar samples, as evidenced in **Figure 20(a)** corresponding to zero freeze-thaw cycles. Importantly, the enhanced pore network synergizes with the thermoregulatory effects of the MPCM's latent heat of fusion to act as expansion reservoirs for freezing water, further enhancing the frost resistance of MPCM-integrated mortars [67,84]. After the freeze-thaw cycle, there is a notable increase in the volume of pores and cracks within the mortar samples, with the control mortar experiencing a much higher increase in porosity. In contrast, the PCM-10 sample showed a minor increase in the volume of pores and cracks, while PCM-20 presented negligible changes. For a quantitative comparison, **Figure 20(b)** shows the % change in the pore/crack volume occurring due to freeze-thaw cycles. **Figure 20(b)** shows about a 30% increase in pores and crack volume within the control mortar after 324 cycles, whereas PCM-10 and PCM-20 exhibited only an 11% and 5% increase, respectively after the same number of freeze-thaw cycles. As discussed, the beneficial effects of MPCM, such as thermal buffering and increased porosity, likely contributed to the observed differences in the response to freeze-thaw cycles.

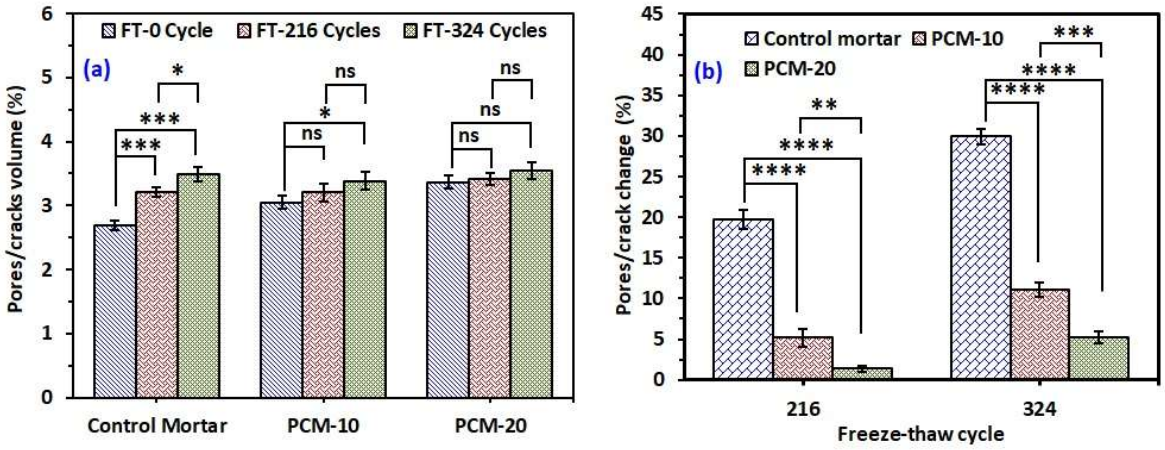

Figure 20. Evolution of (a) percentage of pore/crack volume and (b) percentage change in pore/crack volume in mortar samples with increasing freeze-thaw cycles. Both graphs underscore the enhanced durability imparted by MPCM, with PCM-20 exhibiting the most significant resistance to freeze-thaw-induced damage. (Note: ns $p > 0.05$; * $p \leq 0.05$; ** $p \leq 0.01$; *** $p \leq 0.001$; **** $p \leq 0.0001$).

3.2 Simulation Results

Macro scale simulation results and the resultant FTCs

A comparison of the temperature field across the modeled bridge deck between the control bridge deck without any protective layer and the MPCMC-layer-protected deck is shown in Fig. 21 (a) and (b), respectively. For this specific case, the volume fraction of PCM is set to be 5%, the PCM transition temperature is considered as -5 °C, and the protective layer thickness is taken as 36 mm. The inquiry time is selected to be the night of January 25th, 2017. It can be seen from the temperature fields that the deck with the proposed protective layer has more gradual temperature variation across the whole deck. The overall temperature is higher than the one without any overlay. Moreover, the bridge deck sensory point on the midspan of the cantilever wing shows the most distinct temperature differences. The bridge-top query point temperature without protection shows a temperature of -6.51°C, which is below the freezing temperature of -5.5°C, by assuming a 7% concentration of NaCl in the entrapped saline water in the concrete due to the deicing processes [28,92,93]. Moreover, one can see from the temperature field on the cantilever wing that there is a depth of about 6.25 cm of the control unprotected concrete deck below the freezing temperature. Such a low temperature with a depth indicates a potential freezing cycle.

On the contrary, the identical inquiry point temperature is -5.26°C with the protection of the MPCMC layer. The results suggest that the added layer not only helps the surface temperature to be above the freezing point but also reduces the chance of freezing for the whole depth of the cantilever wing. Moreover, a closer examination confirms that the temperature of the upper part of the bridge deck is increased. This results from the reduced thermal conductivity and the incorporated latent heat effect provided by the protective layer. From the temperature-time histories obtained from the inquiry points between the protected and unprotected bridge decks, we can observe that the added protective layer can effectively reduce the temperature variation of the bridge surface and, for some suitable cases, can prevent freezing, thereby reducing the overall FTCs as can be observed in Fig. 21 (c). More specifically, Fig. 21 (c1) shows the overall temperature-time history. Fig. 21 (c2) and (c3) offer close-up views that illustrate a crucial contrast between the control concrete deck and the bridge deck that features a PCM layer. Specifically, these figures indicate that, in certain scenarios, the temperature of the control deck drops to or below freezing while the temperature of the deck with the PCM layer remains above freezing. This difference in temperature profiles provides evidence of the efficacy of the proposed MPCMC protective layer, which is able to significantly reduce the number of FTCs.

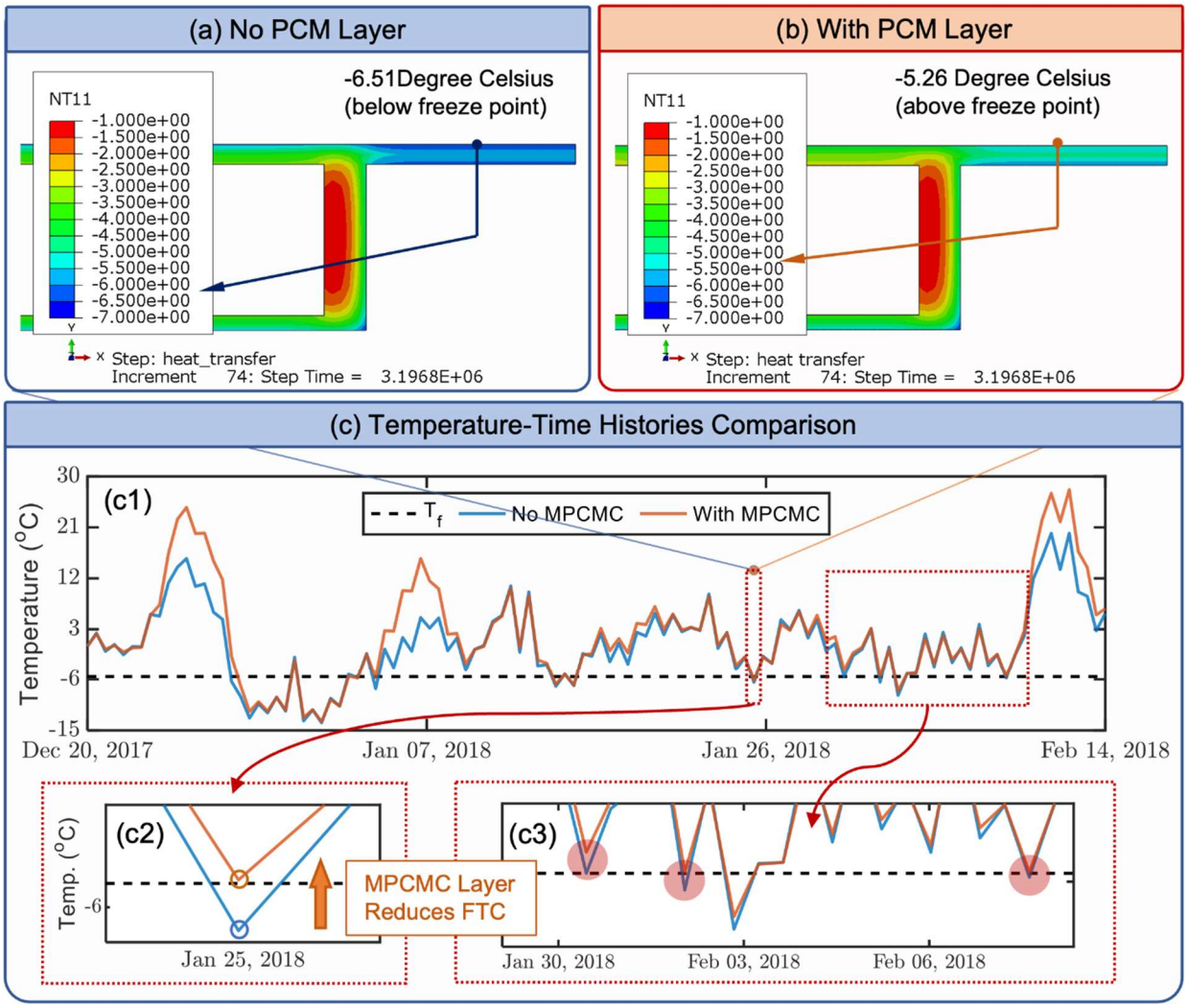

Fig. 21 The effectiveness of the proposed MPCMC protective layer by comparing the control case with respect to an exemplary layer with design parameters: $d_{\text{pcm}} = 8\text{e}^{-6}\text{m}$, $v_{\text{pcm}} = 0.05$, $\rho_{\text{eff}} = 2213\ \text{kg/m}^3$, $k_{\text{eff}} = 1.21\text{W/m·K}$, $C_{\text{peff}} = 908.9\text{J/kg·K}$, $t_{\text{ol}} = 0.036\text{m}$, $H = 250\text{kJ/kg·K}$, and $T_t = -5$. (a) The temperature field without the MPCMC; (b) the temperature field with the exemplary MPCMC; (c) a comparison of the temperature-time histories with and without the MPCMC layer with close-ups that illustrate the FTC reduction about the freezing temperature T_f. Figure c1 shows the overall temperature-time histories. Figures c2 and c3 show close-ups of the Figure c1 at two different time ranges.

Predicted Response from the Trained Intelligent Model and its Interpretation

Predictive performance of the ML model

After tuning the hyperparameters of the FNN, the intelligent model is trained on the training data set and tested on the testing data set. The learning curve is shown in Fig. 22 (a), where it can be seen that the training error kept on decreasing, whereas the testing error remained almost unchanged after the first 700 epochs. Further adjustment to the FNN induces significant

overfitting. Therefore, the best-performing model based on the tuned hyperparameters is characterized by the weights and biases, which are finalized for model evaluation.

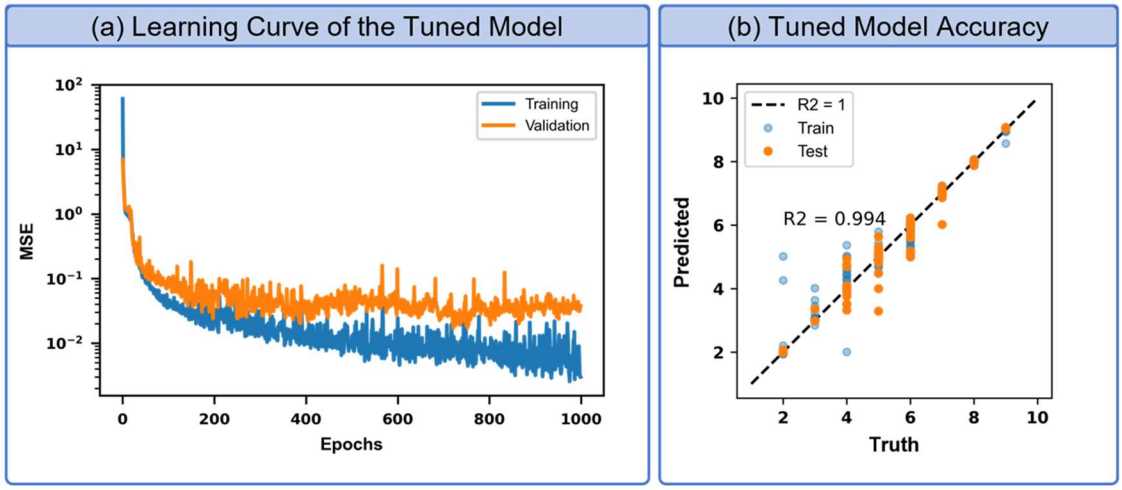

Fig. 22 A schematic of the main contributions of the thermal interaction between the bridge deck and the surrounding: (a) learning curve of the tuned model; (b) tuned model accuracy

In Fig. 22 (b), the accuracy of the training and the testing set is compared with the ideal correlation line, where the explained variance $R^2 = 1$, rendered in the black dashed line. It can be observed that both the training and the testing set agree with the underlying ground truths. Especially for the most extreme cases, the predicted FTCs are almost on top of the ground truths, indicating the FNN-based intelligent model is able to capture the complex input-output mapping. A banded estimate region can be seen in between four to six FTCs. This can be explained by the fact that the considered cycles are defined in whole numbers $FTC \in \mathbb{z}^+$ whereas the predicted FTCs are mapped continuously $\widehat{FTC} \in \mathbb{R}$. Hence, a one-day band indicates very high prediction accuracy if the ceiled values are used as conservative estimates of the FTCs. Quantitatively, the overall accuracy for the test data set can be summarized by an MSE of 0.0134 and an explained variance $R^2 = 0.994$.

3.2.2 SHAP Interpretation of the Predictions

As a direct model evaluation is prohibitive for the FNN intelligent model due to its complexity, the SHAP explainer is used to evaluate the effect of each input feature on the output. Fig. 23 (a) summarizes the attribution of each input feature on affecting the output using the mean estimate of the absolute value of the SHAP and the standard deviation of the SHAP. The mean estimate of the absolute value of SHAP characterizes the average variation irrespective of their direction of contribution. In comparison, the standard deviation characterizes how the SHAP values vary about the mean output. Overall, from Fig. 23 (a), it can be observed that these two metrics show consistent attribution for each input. The overlay thickness affects the output the most among the five inputs followed by the volume fraction, the transition temperature, the diameter of the MPCM, and the latent heat capacity.

To elucidate more on the relative importance of the input features, Fig. 23 (b) shows the violin plots of the SHAP values for the individual input features that contributed to the prediction of the FTC counts. The color scale from blue to red shows the range of values of the individual input

feature, and the horizontal axis shows the SHAP values. While the red color represents the highest input feature value, the blue color represents the lowest value of the input feature. The mean number of FTCs of the entire dataset at 6.37 Celsius is represented by a SHAP value of zero. The features from top-down are arranged in descending order of importance**.**

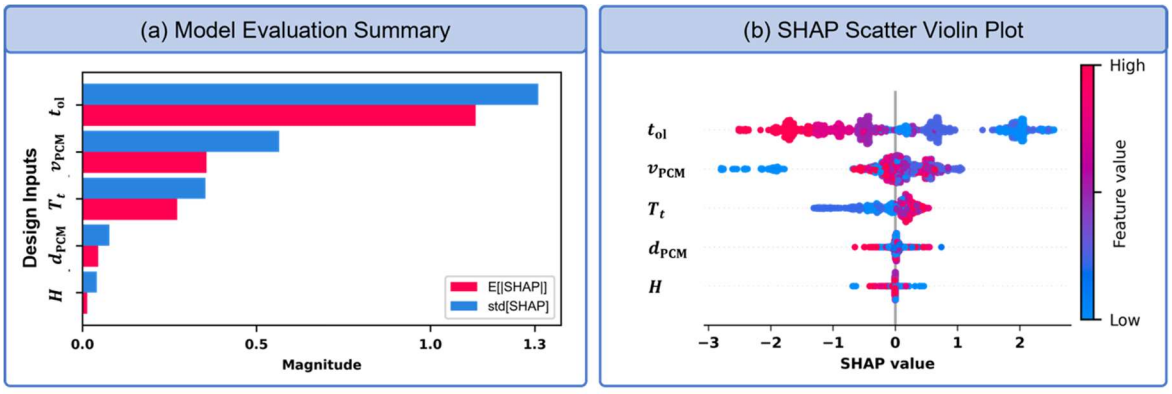

Fig. 23 (a) SHAP summary plot and (b) SHAP violin plot for each input from the trained NN model

For overlay thickness (t_{ol}), a monotonic trend is observed (Figure 22(b)). The blue-colored cluster for higher SHAP values indicates that lower thickness values produce a higher number of FTCs. Similarly, the red cluster for negative SHAP values infers that the lowest number of FTCs can be achieved by using a higher value of overlay thickness. Therefore, the overall result with respect to variation in overlay thickness agrees with engineering intuition that the thicker overlay will introduce less temperature variation for the concrete bridge deck. This also relates to an earlier observation on the PCM-incorporated wall thickness's effect on composite concrete pier [94]. Hence, the general trend from the model is able to explain and incorporate the underlying physics. Although the results indicate the dominance of the overlay thickness on the model output, an overlapping blue and purple-colored cluster near the zero SHAP value indicates that the same number of FTCs can be obtained for lower or intermediate values of the overlay thickness. Such a mixed trend reflects interference from the variations in other design parameters. Thus, while the overlay thickness generally shows a dominating influence on the model output, under design circumstances where higher overlay thicknesses are prohibitive for obvious structural self-weight enhancement concerns, the contributions from other design parameters become very important. For the volume fraction of PCMs, a mixed trend is observed where lower values of PCM volume fraction can result in higher or lower values of FTC counts, and higher volume fractions can yield FTC counts that are higher than those obtained corresponding to lower volume fractions, which was also observed by Rodríguez et al. [95] where higher volume fractions of PCMs have been shown to reduce the frost-resistance. As explained earlier, such a mixed trend reflects significant interaction coming from other input features within the design space. This intricate interaction shows that the v_{PCM} may not be a decisive feature since its resultant output FTCs are affected by other features. The attribution of the transition temperature also shows monotonicity; that is, the higher the transition temperature, the higher the FTC counts, and vice versa. The long blue cluster tail at the negative SHAP values indicates that the low transition temperature PCMs can effectively reduce the FTCs. Thus, the overall monotonic trend reflects the importance of PCM transition temperature in influencing the model output, which is consistent with prior experimental and numerical studies [41,42,96]. For the size of the PCMs, a higher diameter of the MPCM induces

both reduction and increment in the FTCs, which suggests that the response with respect to the size of the PCMs is significantly influenced by other features. The latent heat (H) effect generally shows a monotonic trend where a lower H induces higher FTCs which is well-aligned with the physics. However, a blue cluster of points is also observed for lower SHAP values which contradicts the general monotonic trend. This can be attributed to the interference with the other input features as explained earlier. However, it needs to be noted that the influence of both the diameter of the MPCM, and the latent heat capacity is significantly lower than other parameters in determining the number of FTCs. While the lower importance of the MPCM diameter can be attributed to previous findings [33] that indicate the thermal conductivity of the homogenized composite is solely dependent on the volume fraction of PCMs and not the diameter, the reduced significance of the latent heat capacity can be attributed to the limited range examined in this study, which was restricted to the commercially available paraffinic PCMs with a range of 155-250 KJ/kg. Moreover, even if the latent heat capacity range is expanded, the latent heat released during the phase change would still be constrained by the volume fraction of the MPCM [97].

While the SHAP violin plot concentrates on the impact of a selected individual input feature on the model output, the SHAP river flow plot, concentrates on the impact of the different input features on a selected output value [98]. The SHAP river flow plot of the NN model is illustrated in Fig. 24 for the individual FTCs, as the five input features influence them. Here, the expected value of 6.37, indicates that the predicted value from the model would be the mean of all the predicted 8096 FTC counts in the training of the NN model when no information on the input feature values is available. Every line of the SHAP river flow plot corresponds to specific FTCs. The tendency of these FTC lines to sway above or below the expected value line is influenced by the value of the input feature in the model. The color spectrum corresponds to the property value for a given data point. While the red color represents low FTC counts, the blue represents high FTC counts. The order of arrangement of the input features from right to left on the horizontal axis is in decreasing absolute SHAP values.

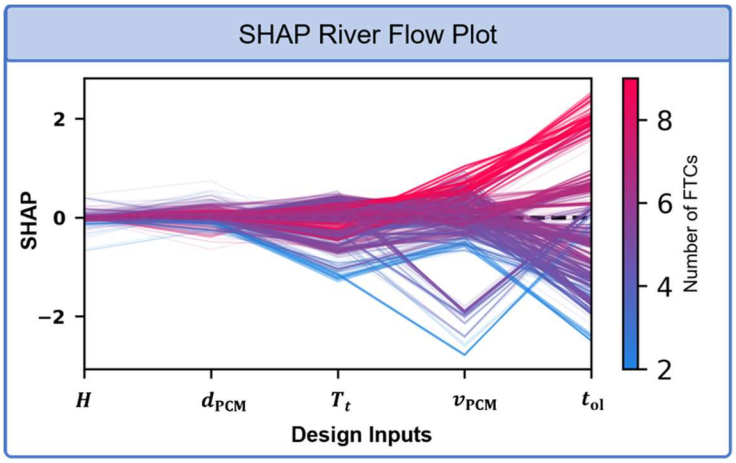

Figure 24. SHAP river flow plot for FTC counts using the trained NN model.

While the SHAP summary and violin plots rank the importance of individual variables and offer their contributions and trends, the river flow plot reveals complex interplay among variables and how they collectively influence FTC outcomes, a level of interaction that cannot be deduced from the SHAP summary or violin plots alone. In Figure 24, the SHAP river flow plot clearly illustrates the interactions among input variables. For example, the higher FTC results are monotonically

contributed by every variable, especially v_{PCM} and t_{ol}. Whereas the cases with approximately 6 FTCs have mixed contribution from the design variables. Even though v_{PCM} has reduced the FTCs significantly, the overlay thickness can still pull the FTC back to a higher level. As for the individual contributions from each of the variables, a monotonic trend is observed for overlay thickness. For lower FTC cases, the overlay thickness tends to reduce the FTC counts below the expected mean value. On the other hand, for higher FTC cases, the overlay thickness tends to increase the FTC counts well above the expected mean value. Thus, the results with respect to overlay thickness suggest that the low FTC cases are primarily contributed by the influence of overlay thickness, whereas high FTC cases correspond to lower contribution from the overlay thickness likely because of significantly lower corresponding overlay thickness values. Among the four features from the lower length scales, PCM transition temperature also showed a monotonic trend. However, the extent of spread was less as compared to the overlay thickness. The rest of the features have not shown significant correlations with the output as t_{ol} or T_t. v_{PCM} has an overall mixed effect on the predicted output, which corresponds well with the observations from the violin plot. The d_{PCM} and H in the river flow plot show an overall mixed trend in the attributed SHAP value with a much narrower spread which signifies that the output value does not change significantly with variations in these parameters, and it stays around the mean.

Generalizability of the Intelligent Model

To illustrate the generalizability of the trained FNN-based intelligent model, model prediction based on the interpolated values and extrapolated values are presented here aside from the trained grid for the input features. The interpolation data is created to examine the generalizability of the FNN model to internal, unseen input combinations. The extrapolation data set is designed to evaluate how well the trained model can extend to complete unseen cases. A wind-rose plot with five axes can characterize the input feature domain and a loop can illustrate a specific combination of design input by connecting the predetermined grids on the axes. Therefore, the FNN model is trained only based on the grid values in the design domain. Fig. 25(a) shows the wind-rose plot for the test inputs. The model is expected to yield reasonably good FTC estimates within the design domain, illustrated by the blue-colored shaded area. A graphical illustration is provided in Fig. 25 (b) to illustrate how to generate the interpolated and extrapolated data sets. To validate the generalizability of the intelligent model, interpolation is conducted using values in between the stipulated grid of the training and testing data sets (see the representation rendered in purple color). For the extrapolated cases, part of the inputs is assigned outside of the training domain, as shown in the red-colored curve.

The results of the model from training/testing data, the interpolated data set, and the extrapolated data set are shown in Fig. 25 (c), (d), and (e), respectively. The trend in the variance bound from the training set shows a wider spread when there are fewer FTCs. When the unseen interpolated samples that may not share the same probability distribution of the train/test data (Fig. 25(d)) are evaluated by the trained, intelligent model and plotted versus the ground truths, it can be observed that most of the cases are predicted within a two-cycle bound except for some outliers and the variance bound follows a similar trend compared to the training data set. Recent advancements in transfer learning [99] present an excellent opportunity for future research to enhance the current framework, potentially improving interpolation accuracy. Moreover, for the extrapolated data set (Fig. 25(e)), the model's predictability remains but with an insensitivity for lower FTC regions,

specifically for FTC counts below three cycles. The variance bound is biased towards more conservative prediction results for low FTC regions. The unseen, zero-FTC samples bias such a trend from the extrapolation process, and such cases correspond to overlay thicknesses with a 20% of extension beyond the currently considered upper limit in overlay thickness. However, it needs to be noted that such higher overlay thickness is impractical when retrofitting existing bridge decks due to the serious concern of increasing the structural self-weight that may interfere with the safety of the structural design. Hence, neglecting such impractical cases of outliers, the interpolation and extrapolation data sets illustrate decent generalizability of the trained, intelligent model that can be extended to realistic unseen design inputs. Overall, the tuned FNN model can serve as a robust reference tool to quickly guide the design parameter selection to yield the optimal reduction in FTCs for bridge deck protection. Potential future research directions to improve the extrapolation accuracy of the developed neural network could involve exploring recently developed generalizable neural network methods [100,101]. Advances in physics-guided Bayesian neural networks [102], which incorporate uncertainty quantification, may offer better extrapolation performance. Additionally, techniques like self-supervised learning [103] could be employed to enhance the model's ability to extrapolate. Investigating these advanced methodologies presents an exciting opportunity to further refine and expand the current framework for better extrapolation accuracy.

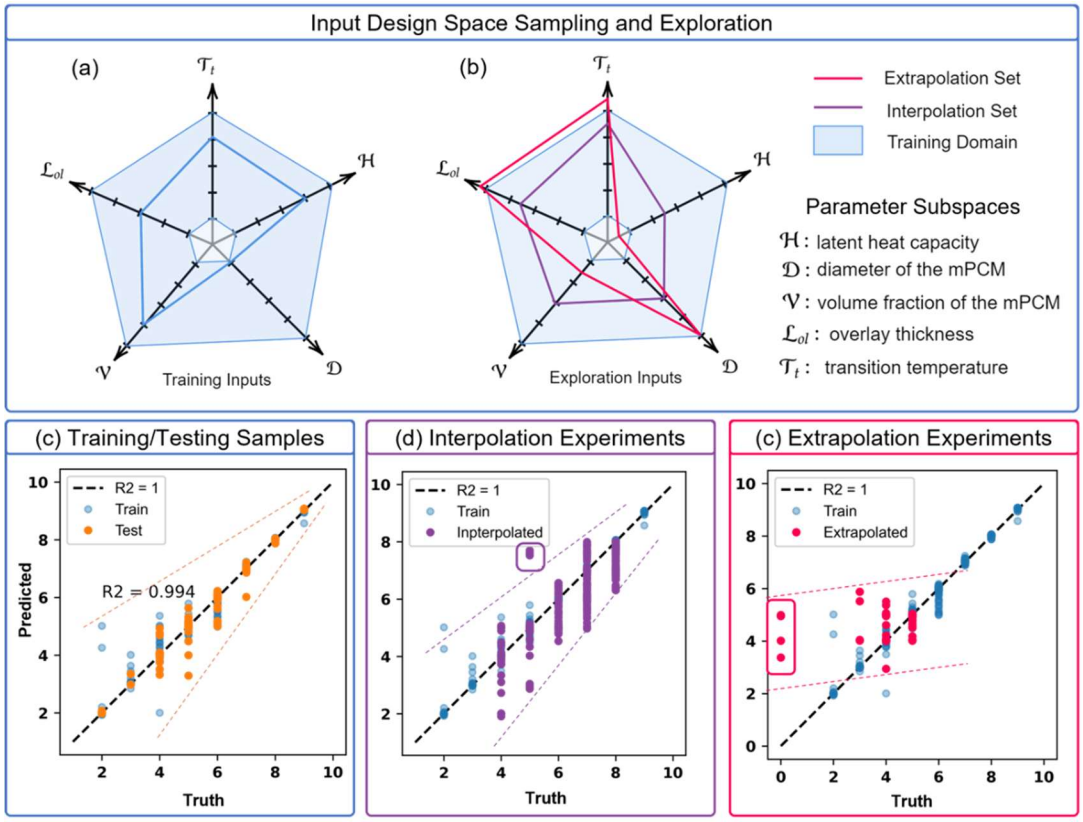

Fig. 25 Generalizability of the Intelligent Model: wind-rose plot for (a) training inputs; (b) exploration inputs (interpolation and extrapolation); performance of the trained model on (c) test dataset, (d) interpolated inputs; (e) extrapolation inputs.

The proposed multiscale simulation and machine-learning guided framework showed a plausible and accurate prediction of the FTCs and optimization of the design parameters. This framework establishes a data-driven explainable testbed for the optimized design of the proposed protective overlay to reduce the FTCs. Moreover, the adaptability of the current framework to other structural geometries and configurations can be further investigated by including geometrical features and related dimensions as variables during dataset creation. Subsequently, implementing these geometrical attributes as inputs to the neural network model presents a promising direction for future research endeavors.

Chapter 5: Conclusions and Recommendations

This project successfully demonstrated the feasibility and effectiveness of incorporating microencapsulated phase change materials (MPCMs) into cementitious systems and concrete overlays to enhance freeze–thaw resistance in bridge and pavement applications. The combined experimental and computational investigations established a comprehensive understanding of how MPCMs improve the thermal, mechanical, and durability performance of concrete exposed to severe winter environments.

The material development and testing confirmed that MPCM integration effectively moderates temperature variations within cementitious composites during freezing conditions. The MPCMs exhibited a high heat of fusion, releasing latent heat within the critical freezing range of approximately 1°C to –18°C, which delayed ice formation and reduced thermal stresses. Mortars containing MPCMs demonstrated substantial improvement in freeze–thaw durability, exhibiting minimal loss of strength and stiffness even after extensive thermal cycling. Advanced imaging and structural analyses further verified enhanced meso-structural stability, with reduced crack development and porosity evolution compared to control materials. These results confirm that MPCM-incorporated cementitious materials offer a reliable pathway to improve frost resistance and extend the service life of concrete in cold climates.

Complementing the experimental findings, the project developed a multiscale simulation and machine learning–based intelligent design framework to guide the optimization of PCM-enhanced concrete overlays. The modeling approach accurately captured the thermal response of bridge decks under location-specific weather conditions and identified key design parameters—particularly layer thickness, PCM volume fraction, and transition temperature—that most strongly influence freeze–thaw mitigation. The predictive model demonstrated high accuracy in estimating the reduction in freeze–thaw cycles and provided interpretable insights into parameter interactions through Shapley-based analysis.

Together, the experimental results and intelligent design framework confirm the technical feasibility and practical promise of MPCM integration as a durable, self-regulating solution for mitigating freeze–thaw damage in transportation infrastructure. The approach enables the rational design of PCM-enhanced concrete mixtures and overlays tailored to regional climatic conditions, providing transportation agencies with a scientifically grounded, data-driven tool for improving the resilience and longevity of bridges and pavements in cold environments.

References

[1] ASTM C150/C150M − 22. Specification for Portland Cement. PA (USA): ASTM International; n.d. https://doi.org/10.1520/C0150_C0150M-22.

[2] Esmaeeli HS, Farnam Y, Haddock JE, Zavattieri PD, Weiss WJ. Numerical analysis of the freeze-thaw performance of cementitious composites that contain phase change material (PCM). Mater Des 2018;145:74–87. https://doi.org/10.1016/j.matdes.2018.02.056.

[3] Farnam Y, Esmaeeli HS, Zavattieri PD, Haddock J, Weiss J. Incorporating phase change materials in concrete pavement to melt snow and ice. Cem Concr Compos 2017;84:134–45. https://doi.org/10.1016/j.cemconcomp.2017.09.002.

[4] Balapour M, Mutua AW, Farnam Y. Evaluating the thermal efficiency of microencapsulated phase change materials for thermal energy storage in cementitious composites. Cem Concr Compos 2021;116:103891. https://doi.org/10.1016/j.cemconcomp.2020.103891.

[5] Tang Q, Sun J, Yu S, Wang G. Improving thermal conductivity and decreasing supercooling of paraffin phase change materials by n-octadecylamine-functionalized multi-walled carbon nanotubes. RSC Adv 2014;4:36584–90. https://doi.org/10.1039/C4RA04225E.

[6] Šavija B, Zhang H, Schlangen E. Influence of Microencapsulated Phase Change Material (PCM) Addition on (Micro) Mechanical Properties of Cement Paste. Materials 2017;10:863. https://doi.org/10.3390/ma10080863.

[7] Romero Rodríguez C, França De Mendonça Filho F, Chaves Figueiredo S, Schlangen E, Šavija B. Fundamental investigation on the frost resistance of mortar with microencapsulated phase change materials. Cem Concr Compos 2020;113:103705. https://doi.org/10.1016/j.cemconcomp.2020.103705.

[8] ASTM C1437 - 20. Standard Test Method for Flow of Hydraulic Cement Mortar n.d.

[9] ASTM C666/C666M − 15. Test Method for Resistance of Concrete to Rapid Freezing and Thawing. PA (USA): ASTM International; n.d. https://doi.org/10.1520/C0666_C0666M-15.

[10] Sharifi NP, Sakulich A. Application of phase change materials to improve the thermal performance of cementitious material. Energy Build 2015;103:83–95. https://doi.org/10.1016/j.enbuild.2015.06.040.

[11] Farnam Y, Krafcik M, Liston L, Washington T, Erk K, Tao B, et al. Evaluating the Use of Phase Change Materials in Concrete Pavement to Melt Ice and Snow. J Mater Civ Eng 2016;28:04015161. https://doi.org/10.1061/(ASCE)MT.1943-5533.0001439.

[12] ASTM C109/C109M − 21. Standard Test Method for Compressive Strength of Hydraulic Cement Mortars (Using 2-in. or [50 mm] Cube Specimens) n.d. https://www.astm.org/c0109_c0109m-20.html.

[13] ASTM C348 − 21. Standard Test Method for Flexural Strength of Hydraulic-Cement Mortars n.d. https://www.astm.org/c0348-21.html.

[14] Wang Y, Yang W, Ge Y, Liu P, Zhang A. Analysis of freeze-thaw damage and pore structure deterioration of mortar by low-field NMR. Constr Build Mater 2022;319:126097. https://doi.org/10.1016/j.conbuildmat.2021.126097.

[15] ZEISS Corp. ZEISS Xradia 610 Versa. Scout-Scan Instrum Control Syst n.d. https://www.zeiss.com/microscopy/us/l/campaigns/scout-and-scan.html (accessed March 18, 2024).

[16] Dragonfly | 3D Visualization and Analysis Solutions for Scientific and Industrial Data | ORS n.d. https://www.theobjects.com/dragonfly/index.html (accessed May 31, 2023).
[17] Kim H-T, Razakamandimby R. DFT, Szilágyi V, Kis Z, Szentmiklósi L, Glinicki MA, et al. Reconstruction of concrete microstructure using complementarity of X-ray and neutron tomography. Cem Concr Res 2021;148:106540. https://doi.org/10.1016/j.cemconres.2021.106540.
[18] Das S, Yang P, Singh SS, Mertens JCE, Xiao X, Chawla N, et al. Effective properties of a fly ash geopolymer: Synergistic application of X-ray synchrotron tomography, nanoindentation, and homogenization models. Cem Concr Res 2015;78:252–62. https://doi.org/10.1016/j.cemconres.2015.08.004.
[19] Iassonov P, Gebrenegus T, Tuller M. Segmentation of X-ray computed tomography images of porous materials: A crucial step for characterization and quantitative analysis of pore structures. Water Resour Res 2009;45. https://doi.org/10.1029/2009WR008087.
[20] Reedy CL, Reedy CL. High-resolution micro-CT with 3D image analysis for porosity characterization of historic bricks. Herit Sci 2022;10:83. https://doi.org/10.1186/s40494-022-00723-4.
[21] Eik M, Antonova A, Puttonen J. Phase contrast tomography to study near-field effects of polypropylene fibres on hardened cement paste. Cem Concr Compos 2020;114:103800. https://doi.org/10.1016/j.cemconcomp.2020.103800.
[22] Zhang M, He Y, Ye G, Lange DA, Breugel K van. Computational investigation on mass diffusivity in Portland cement paste based on X-ray computed microtomography (μCT) image. Constr Build Mater 2012;27:472–81. https://doi.org/10.1016/j.conbuildmat.2011.07.017.
[23] Zhang H, Šavija B, Chaves Figueiredo S, Lukovic M, Schlangen E. Microscale Testing and Modelling of Cement Paste as Basis for Multi-Scale Modelling. Materials 2016;9:907. https://doi.org/10.3390/ma9110907.
[24] Shakoorioskooie M, Griffa M, Leemann A, Zboray R, Lura P. Alkali-silica reaction products and cracks: X-ray micro-tomography-based analysis of their spatial-temporal evolution at a mesoscale. Cem Concr Res 2021;150:106593. https://doi.org/10.1016/j.cemconres.2021.106593.
[25] Li N, Zhao Y, Xing Y, He X. Localized Damage Analysis of Cement Mortar Using X-ray Computed Tomography In Situ Compressive Loading and Digital Volume Correlation. Appl Sci 2023;13:3842. https://doi.org/10.3390/app13063842.
[26] Lubachevsky BD, Stillinger FH. Geometric properties of random disk packings. J Stat Phys 1990;60:561–83. https://doi.org/10.1007/BF01025983.
[27] Lubachevsky BD, Stillinger FH, Pinson EN. Disks vs. spheres: Contrasting properties of random packings. J Stat Phys 1991;64:501–24. https://doi.org/10.1007/BF01048304.
[28] Nayak S, Lyngdoh GA, Das S. Influence of microencapsulated phase change materials (PCMs) on the chloride ion diffusivity of concretes exposed to Freeze-thaw cycles: Insights from multiscale numerical simulations. Constr Build Mater 2019;212:317–28. https://doi.org/10.1016/j.conbuildmat.2019.04.003.
[29] Nayak S, Krishnan NMA, Das S. Microstructure-guided numerical simulation to evaluate the influence of phase change materials (PCMs) on the freeze-thaw response of concrete pavements. Constr Build Mater 2019;201:246–56. https://doi.org/10.1016/j.conbuildmat.2018.12.199.

[30] Lyngdoh GA, Zaki M, Krishnan NMA, Das S. Prediction of concrete strengths enabled by missing data imputation and interpretable machine learning. Cem Concr Compos 2022;128:104414. https://doi.org/10.1016/j.cemconcomp.2022.104414.
[31] Sanahuja J, Toulemonde C. Numerical homogenization of concrete microstructures without explicit meshes. Cem Concr Res 2011;41:1320–9. https://doi.org/10.1016/j.cemconres.2011.03.023.
[32] Mohsen Karimian SA, Straatman AG. A thermal periodic boundary condition for heating and cooling processes. Int J Heat Fluid Flow 2007;28:329–39. https://doi.org/10.1016/j.ijheatfluidflow.2006.03.023.
[33] Thiele AM, Kumar A, Sant G, Pilon L. Effective thermal conductivity of three-component composites containing spherical capsules. Int J Heat Mass Transf 2014;73:177–85. https://doi.org/10.1016/j.ijheatmasstransfer.2014.02.002.
[34] Jurkowska M, Szczygieł I. Review on properties of microencapsulated phase change materials slurries (mPCMS). Appl Therm Eng 2016;98:365–73. https://doi.org/10.1016/j.applthermaleng.2015.12.051.
[35] Salaün F, Vroman I. Influence of core materials on thermal properties of melamine–formaldehyde microcapsules. Eur Polym J 2008;44:849–60. https://doi.org/10.1016/j.eurpolymj.2007.11.018.
[36] Assael MJ, Botsios S, Gialou K, Metaxa IN. Thermal Conductivity of Polymethyl Methacrylate (PMMA) and Borosilicate Crown Glass BK7. Int J Thermophys 2005;26:1595–605. https://doi.org/10.1007/s10765-005-8106-5.
[37] Rouabah F, Dadache D, Haddaoui N. Thermophysical and Mechanical Properties of Polystyrene: Influence of Free Quenching. ISRN Polym Sci 2012;2012:e161364. https://doi.org/10.5402/2012/161364.
[38] Chen S, Cheng X, Li Y, Wang X, Zheng H, Zhong H. Study on the microstructures and thermal properties of SiO2@NaNO3 microcapsule thermal storage materials. Int J Energy Res 2020;44:10008–22. https://doi.org/10.1002/er.5566.
[39] Ji W, Cheng X, Chen H, Li L, Li Y, Liu Z. Efficient synthesis of regular spherical GO/SiO2@Solar Salt microcapsules to enhance heat-storage capacity and cycle stability. Energy Convers Manag 2021;245:114637. https://doi.org/10.1016/j.enconman.2021.114637.
[40] Rubitherm GmbH n.d. https://www.rubitherm.eu/en/productcategory/organische-pcm-rt (accessed July 29, 2022).
[41] Yeon JH, Kim K-K. Potential applications of phase change materials to mitigate freeze-thaw deteriorations in concrete pavement. Constr Build Mater 2018;177:202–9. https://doi.org/10.1016/j.conbuildmat.2018.05.113.
[42] Yeon JH. Thermal behavior of cement mortar embedded with low-phase transition temperature PCM. Constr Build Mater 2020;252:119168. https://doi.org/10.1016/j.conbuildmat.2020.119168.
[43] Thiele AM, Sant G, Pilon L. Diurnal thermal analysis of microencapsulated PCM-concrete composite walls. Energy Convers Manag 2015;93:215–27. https://doi.org/10.1016/j.enconman.2014.12.078.
[44] PlusICE Organic Range 2021-1 n.d.
[45] Branco FA, Mendes PA. Thermal Actions for Concrete Bridge Design. J Struct Eng 1993;119:2313–31. https://doi.org/10.1061/(ASCE)0733-9445(1993)119:8(2313).

[46] Zhou G-D, Yi T-H. Thermal Load in Large-Scale Bridges: A State-of-the-Art Review. Int J Distrib Sens Netw 2013;9:217983. https://doi.org/10.1155/2013/217983.
[47] Mirambell E, Aguado A. Temperature and Stress Distributions in Concrete Box Girder Bridges. J Struct Eng 1990;116:2388–409. https://doi.org/10.1061/(ASCE)0733-9445(1990)116:9(2388).
[48] Abid SR, Tayşi N, Özakça M. Experimental analysis of temperature gradients in concrete box-girders. Constr Build Mater 2016;106:523–32. https://doi.org/10.1016/j.conbuildmat.2015.12.144.
[49] Liu Z, Hou J, Meng X, Dewancker BJ. A numerical study on the effect of phase-change material (PCM) parameters on the thermal performance of lightweight building walls. Case Stud Constr Mater 2021;15:e00758. https://doi.org/10.1016/j.cscm.2021.e00758.
[50] Urgessa G, Yun K-K, Yeon J, Yeon JH. Thermal responses of concrete slabs containing microencapsulated low-transition temperature phase change materials exposed to realistic climate conditions. Cem Concr Compos 2019;104:103391. https://doi.org/10.1016/j.cemconcomp.2019.103391.
[51] NSRDB n.d. https://nsrdb.nrel.gov/ (accessed September 6, 2022).
[52] Cybenko G. Approximation by superpositions of a sigmoidal function. Math Control Signals Syst 1989;2:303–14. https://doi.org/10.1007/BF02551274.
[53] Lyngdoh GA, Li H, Zaki M, Krishnan NMA, Das S. Elucidating the constitutive relationship of calcium–silicate–hydrate gel using high throughput reactive molecular simulations and machine learning. Sci Rep 2020;10:21336. https://doi.org/10.1038/s41598-020-78368-1.
[54] Liang M, Chang Z, Wan Z, Gan Y, Schlangen E, Šavija B. Interpretable Ensemble-Machine-Learning models for predicting creep behavior of concrete. Cem Concr Compos 2022;125:104295. https://doi.org/10.1016/j.cemconcomp.2021.104295.
[55] Wilson PW, Arthur JW, Haymet ADJ. Ice Premelting during Differential Scanning Calorimetry. Biophys J 1999;77:2850–5. https://doi.org/10.1016/S0006-3495(99)77116-X.
[56] Yao Y, Fella V, Huang W, Zhang KAI, Landfester K, Butt H-J, et al. Crystallization and Dynamics of Water Confined in Model Mesoporous Silica Particles: Two Ice Nuclei and Two Fractions of Water. Langmuir 2019;35:5890–901. https://doi.org/10.1021/acs.langmuir.9b00496.
[57] Morishige K, Iwasaki H. X-ray Study of Freezing and Melting of Water Confined within SBA-15. Langmuir 2003;19:2808–11. https://doi.org/10.1021/la0208474.
[58] Knight AW, Kalugin NG, Coker E, Ilgen AG. Water properties under nano-scale confinement. Sci Rep 2019;9:8246. https://doi.org/10.1038/s41598-019-44651-z.
[59] Bednarska D, Koniorczyk M. Freezing of partly saturated cementitious materials – Insight into properties of pore confined solution and microstructure. Constr Build Mater 2020;251:118895. https://doi.org/10.1016/j.conbuildmat.2020.118895.
[60] Rjiba A, Khoder H, Jelassi J, Bouguet-Bonnet S, Gardiennet C, Bendeif E-E, et al. Differential scanning calorimetry and NMR study of water confined in a mesoporous bioactive glass. Microporous Mesoporous Mater 2021;316:110922. https://doi.org/10.1016/j.micromeso.2021.110922.
[61] Bager DH, Sellevold EJ. Ice formation in hardened cement paste, Part I — room temperature cured pastes with variable moisture contents. Cem Concr Res 1986;16:709–20. https://doi.org/10.1016/0008-8846(86)90045-1.

[62] Snyder KA, Bentz DP. Suspended hydration and loss of freezable water in cement pastes exposed to 90% relative humidity n.d.
[63] Ridi F, Luciani P, Fratini E, Baglioni P. Water Confined in Cement Pastes as a Probe of Cement Microstructure Evolution. J Phys Chem B 2009;113:3080–7. https://doi.org/10.1021/jp808754t.
[64] Eddhahak-Ouni A, Drissi S, Colin J, Neji J, Care S. Experimental and multi-scale analysis of the thermal properties of Portland cement concretes embedded with microencapsulated Phase Change Materials (PCMs). Appl Therm Eng 2014;64:32–9. https://doi.org/10.1016/j.applthermaleng.2013.11.050.
[65] Jayalath A, San Nicolas R, Sofi M, Shanks R, Ngo T, Aye L, et al. Properties of cementitious mortar and concrete containing micro-encapsulated phase change materials. Constr Build Mater 2016;120:408–17. https://doi.org/10.1016/j.conbuildmat.2016.05.116.
[66] Han P, Qiu X, Lu L, Pan L. Fabrication and characterization of a new enhanced hybrid shell microPCM for thermal energy storage. Energy Convers Manag 2016;126:673–85. https://doi.org/10.1016/j.enconman.2016.08.052.
[67] Pilehvar S, Cao VD, Szczotok AM, Valentini L, Salvioni D, Magistri M, et al. Mechanical properties and microscale changes of geopolymer concrete and Portland cement concrete containing micro-encapsulated phase change materials. Cem Concr Res 2017;100:341–9. https://doi.org/10.1016/j.cemconres.2017.07.012.
[68] Cui H, Liao W, Mi X, Lo TY, Chen D. Study on functional and mechanical properties of cement mortar with graphite-modified microencapsulated phase-change materials. Energy Build 2015;105:273–84. https://doi.org/10.1016/j.enbuild.2015.07.043.
[69] Paswan R, Das S. Elucidating the evolution of pore structure, microstructural damage, and micromechanical response in cement pastes containing microencapsulated phase change materials under freeze-thaw conditions. Cem Concr Compos 2024;154:105743. https://doi.org/10.1016/j.cemconcomp.2024.105743.
[70] El Moustapha B, Bonnet S, Khelidj A, Maranzana N, Froelich D, Khalifa A, et al. Effects of microencapsulated phase change materials on chloride ion transport properties of geopolymers incorporating slag and, metakaolin, and cement-based mortars. J Build Eng 2023;74:106887. https://doi.org/10.1016/j.jobe.2023.106887.
[71] Aguayo M, Das S, Maroli A, Kabay N, Mertens JCE, Rajan SD, et al. The influence of microencapsulated phase change material (PCM) characteristics on the microstructure and strength of cementitious composites: Experiments and finite element simulations. Cem Concr Compos 2016;73:29–41. https://doi.org/10.1016/j.cemconcomp.2016.06.018.
[72] Fernandes F, Manari S, Aguayo M, Santos K, Oey T, Wei Z, et al. On the feasibility of using phase change materials (PCMs) to mitigate thermal cracking in cementitious materials. Cem Concr Compos 2014;51:14–26. https://doi.org/10.1016/j.cemconcomp.2014.03.003.
[73] Šavija B, Schlangen E. Use of phase change materials (PCMs) to mitigate early age thermal cracking in concrete: Theoretical considerations. Constr Build Mater 2016;126:332–44. https://doi.org/10.1016/j.conbuildmat.2016.09.046.
[74] Falzone G, Falla GP, Wei Z, Zhao M, Kumar A, Bauchy M, et al. The influences of soft and stiff inclusions on the mechanical properties of cementitious composites. Cem Concr Compos 2016;71:153–65. https://doi.org/10.1016/j.cemconcomp.2016.05.008.

[75] Xu Y, Yuan Q, Dai X, Xiang G. Improving the freeze-thaw resistance of mortar by a combined use of superabsorbent polymer and air entraining agent. J Build Eng 2022;52:104471. https://doi.org/10.1016/j.jobe.2022.104471.
[76] Nayak S, Lyngdoh GA, Das S. Influence of microencapsulated phase change materials (PCMs) on the chloride ion diffusivity of concretes exposed to Freeze-thaw cycles: Insights from multiscale numerical simulations. Constr Build Mater 2019;212:317–28. https://doi.org/10.1016/j.conbuildmat.2019.04.003.
[77] Valenza II JJ, Scherer GW. Mechanism for Salt Scaling. J Am Ceram Soc 2006;89:1161–79. https://doi.org/10.1111/j.1551-2916.2006.00913.x.
[78] Neville AM. Properties of concrete. 5th ed. Harlow, England ; New York: Pearson; 2011.
[79] Vancura M, MacDonald K, Khazanovich L. Microscopic analysis of paste and aggregate distresses in pervious concrete in a wet, hard freeze climate. Cem Concr Compos 2011;33:1080–5. https://doi.org/10.1016/j.cemconcomp.2011.05.011.
[80] Basheer L, Kropp J, Cleland DJ. Assessment of the durability of concrete from its permeation properties: a review. Constr Build Mater 2001;15:93–103. https://doi.org/10.1016/S0950-0618(00)00058-1.
[81] Mehta PK, Monteiro PJM. Concrete: microstructure, properties, and materials. 3rd ed. New York: McGraw-Hill; 2006.
[82] Hunger M, Entrop AG, Mandilaras I, Brouwers HJH, Founti M. The behavior of self-compacting concrete containing micro-encapsulated Phase Change Materials. Cem Concr Compos 2009;31:731–43. https://doi.org/10.1016/j.cemconcomp.2009.08.002.
[83] Dehdezi PK, Hall MR, Dawson AR, Casey SP. Thermal, mechanical and microstructural analysis of concrete containing microencapsulated phase change materials. Int J Pavement Eng 2013;14:449–62. https://doi.org/10.1080/10298436.2012.716837.
[84] Pilehvar S, Szczotok AM, Rodríguez JF, Valentini L, Lanzón M, Pamies R, et al. Effect of freeze-thaw cycles on the mechanical behavior of geopolymer concrete and Portland cement concrete containing micro-encapsulated phase change materials. Constr Build Mater 2019;200:94–103. https://doi.org/10.1016/j.conbuildmat.2018.12.057.
[85] Liu F, Tang R, Ma W, Yuan X. Frost Resistance and Meso-deterioration Analysis of Microcapsulated Phase Change Materials Modified Concrete. J Build Eng 2022;61:105214. https://doi.org/10.1016/j.jobe.2022.105214.
[86] Yang X, Shen A, Guo Y, Zhou S, He T. Deterioration mechanism of interface transition zone of concrete pavement under fatigue load and freeze-thaw coupling in cold climatic areas. Constr Build Mater 2018;160:588–97. https://doi.org/10.1016/j.conbuildmat.2017.11.031.
[87] Essid N, Loulizi A, Neji J. Compressive strength and hygric properties of concretes incorporating microencapsulated phase change material. Constr Build Mater 2019;222:254–62. https://doi.org/10.1016/j.conbuildmat.2019.06.156.
[88] Wang R, Hu Z, Li Y, Wang K, Zhang H. Review on the deterioration and approaches to enhance the durability of concrete in the freeze–thaw environment. Constr Build Mater 2022;321:126371. https://doi.org/10.1016/j.conbuildmat.2022.126371.
[89] Ebrahimi K, Daiezadeh MJ, Zakertabrizi M, Zahmatkesh F, Habibnejad Korayem A. A review of the impact of micro- and nanoparticles on freeze-thaw durability of hardened concrete: Mechanism perspective. Constr Build Mater 2018;186:1105–13. https://doi.org/10.1016/j.conbuildmat.2018.08.029.

[90] Nayak S, Krishnan NMA, Das S. Microstructure-guided numerical simulation to evaluate the influence of phase change materials (PCMs) on the freeze-thaw response of concrete pavements. Constr Build Mater 2019;201:246–56. https://doi.org/10.1016/j.conbuildmat.2018.12.199.
[91] Li H-W-X, Lyngdoh G, Krishnan NMA, Das S. Machine learning guided design of microencapsulated phase change materials-incorporated concretes for enhanced freeze-thaw durability. Cem Concr Compos 2023;140:105090. https://doi.org/10.1016/j.cemconcomp.2023.105090.
[92] Farnam Y, Bentz D, Hampton A, Weiss WJ. Acoustic Emission and Low-Temperature Calorimetry Study of Freeze and Thaw Behavior in Cementitious Materials Exposed to Sodium Chloride Salt. Transp Res Rec 2014;2441:81–90. https://doi.org/10.3141/2441-11.
[93] Esmaeeli HS, Farnam Y, Haddock JE, Zavattieri PD, Weiss WJ. Numerical analysis of the freeze-thaw performance of cementitious composites that contain phase change material (PCM). Mater Des 2018;145:74–87. https://doi.org/10.1016/j.matdes.2018.02.056.
[94] Tian Y, Lai Y, Qin Z, Pei W. Numerical investigation on the thermal control performance and freeze-thaw resistance of a composite concrete pier with microencapsulated phase change materials. Sol Energy 2022;231:970–84. https://doi.org/10.1016/j.solener.2021.12.042.
[95] Romero Rodríguez C, França de Mendonça Filho F, Chaves Figueiredo S, Schlangen E, Šavija B. Fundamental investigation on the frost resistance of mortar with microencapsulated phase change materials. Cem Concr Compos 2020;113:103705. https://doi.org/10.1016/j.cemconcomp.2020.103705.
[96] Bentz DP, Turpin R. Potential applications of phase change materials in concrete technology. Cem Concr Compos 2007;29:527–32. https://doi.org/10.1016/j.cemconcomp.2007.04.007.
[97] Rathod MK, Banerjee J. Thermal stability of phase change materials used in latent heat energy storage systems: A review. Renew Sustain Energy Rev 2013;18:246–58. https://doi.org/10.1016/j.rser.2012.10.022.
[98] Bhattoo R, Bishnoi S, Zaki M, Krishnan NMA. Understanding the compositional control on electrical, mechanical, optical, and physical properties of inorganic glasses with interpretable machine learning. Acta Mater 2023;242:118439. https://doi.org/10.1016/j.actamat.2022.118439.
[99] Ma J, Cheng JCP, Ding Y, Lin C, Jiang F, Wang M, et al. Transfer learning for long-interval consecutive missing values imputation without external features in air pollution time series. Adv Eng Inform 2020;44:101092. https://doi.org/10.1016/j.aei.2020.101092.
[100] Zhu M, Zhang H, Jiao A, Karniadakis GE, Lu L. Reliable extrapolation of deep neural operators informed by physics or sparse observations 2022. https://doi.org/10.48550/arXiv.2212.06347.
[101] Cai S, Wang Z, Wang S, Perdikaris P, Karniadakis GE. Physics-Informed Neural Networks for Heat Transfer Problems. J Heat Transf 2021;143. https://doi.org/10.1115/1.4050542.
[102] Fernández J, Chiachío J, Chiachío M, Barros J, Corbetta M. Physics-guided Bayesian neural networks by ABC-SS: Application to reinforced concrete columns. Eng Appl Artif Intell 2023;119:105790. https://doi.org/10.1016/j.engappai.2022.105790.

[103] Yang K, Cao Y, Zhang Y, Fan S, Tang M, Aberg D, et al. Self-supervised learning and prediction of microstructure evolution with convolutional recurrent neural networks. Patterns 2021;2:100243. https://doi.org/10.1016/j.patter.2021.100243.

Transportation Infrastructure Durability Center
AT THE UNIVERSITY OF MAINE

35 Flagstaff Road
Orono, Maine 04469
tidc@maine.edu
207.581.4376

www.tidc-utc.org